SUPPLEMENTAL INFORMATION

SUPPLEMENTAL FIGURES

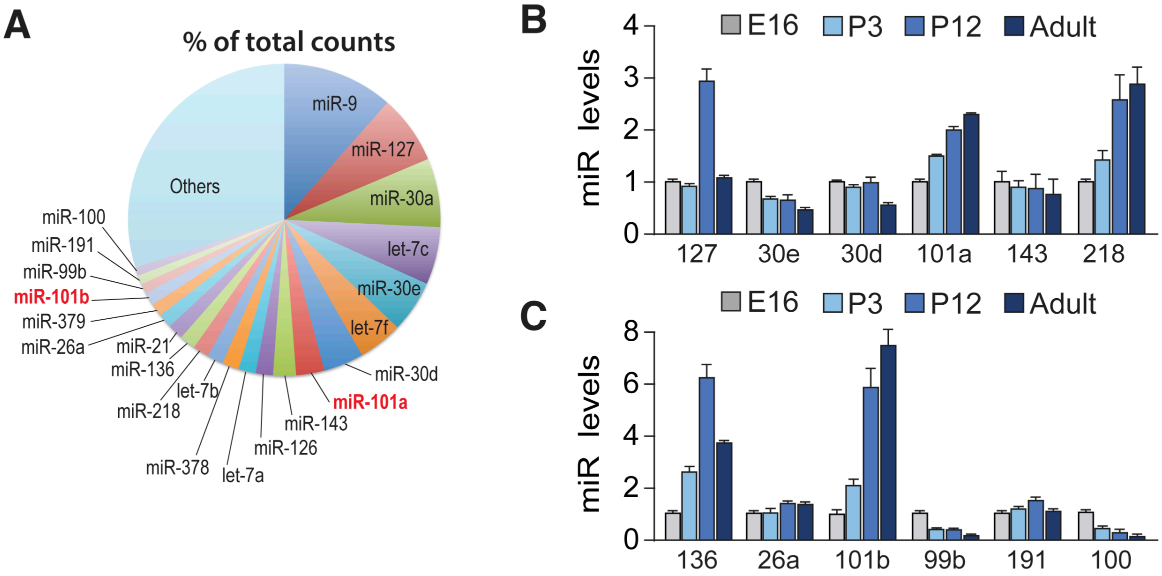

D

Functional annotation of miR-101 HITS-CLIP targets (DAVID)

Biological Theme	FDR	% of all miR-101 targets	Fold Enrichment	P Value
Transmission of nerve impulse	0.00	3.83	3.30	1.9E-06
Embryonic development	0.05	3.83	2.79	2.7E-05
Synaptic transmission	0.06	3.00	3.28	3.5E-05
Forebrain development	0.10	2.83	3.30	5.7E-05
Cell motion	0.30	4.33	2.30	1.8E-04
Regulation of cytoskeleton organization	0.39	2.00	3.93	2.3E-04
Cell-cell signaling	0.44	3.67	2.46	2.6E-04
Embryonic development ending in birth	0.52	4.67	2.14	3.0E-04
Adult locomotory behavior	1.01	1.50	4.71	5.9E-04
Chordate embryonic development	1.03	4.50	2.08	6.0E-04
Negative regulation of cytoskeleton organization	1.05	1.33	5.40	6.1E-04
TGF beta receptor signaling pathway	1.05	1.33	5.40	6.1E-04
Behavior	1.31	4.33	2.08	7.7E-04
Ion transport	2.14	6.33	1.73	1.3E-03
Potassium ion transport	2.27	2.33	2.84	1.3E-03
Regulation of action potential in neuron	4.05	1.17	5.04	2.4E-03
Cell migration	5.23	2.83	2.30	3.1E-03
Regulation of MAP kinase activity	7.04	1.50	3.47	4.2E-03
Ion homeostasis	7.06	3.17	2.10	4.3E-03

Figure S1. Features identifying miR-101 as a top candidate for mediating a major transition in early brain development. Related to Figure 1. (A) Pie chart showing the proportion of total sequenced reads obtained from small RNA deep sequencing (Illumina) for the indicated miRs in P12 hippocampus (data averaged for 6 wild-type animals). (B and C) Twelve of the most expressed miRs were chosen and their developmental regulation tested. (Excluded at this stage were miRs such as miR-9 and the let-7 family that are known to be highly expressed during embryonic life and thought to affect stem cell renewal and early differentiation; Bian et al., 2011). The bar graphs represent the abundance of each miR at P3, P12, and adult (> P40), normalized first for housekeeping gene snoRNA-412 and then for the amount present at embryonic day (E) 16, as assessed by qPCR analysis. Four candidates showed increased expression levels during the relevant developmental window (E16-P12): miR-127, miR-101a and b, and miR-218. Of these four, only miR-101 was reported to be highly enriched in Ago-miR-mRNA complexes as measured by HITS-CLIP experiments in the cortex at P13 (Chi et al., 2009), suggesting that miR-101 is preferentially loaded in the RISC complex that mediates post-transcriptional repression. The miR-101a and b isoforms differ by only one nucleotide (Figure S2H) and have identical seed sequence. (D) Putative targets of miR-101 derived from the HITS-CLIP database (Chi et al., 2009) were functionally annotated through DAVID and ordered by ascending false discovery rate (FDR). Also listed is the % of all miR-101 targets for that biological theme, and fold-enrichment compared to the entire mouse transcriptome (see Supplemental Experimental Procedures). MiR-101a and b are relatively abundant and enriched in the Ago complex (consistent with Chi et al., 2009; Eacker et al., 2011; Zongaro et al., 2013), increase substantially during the relevant time window (consistent with Zongaro et al., 2013), and have potential targets highly relevant for neuronal development, making them top candidates for mediating the transition.

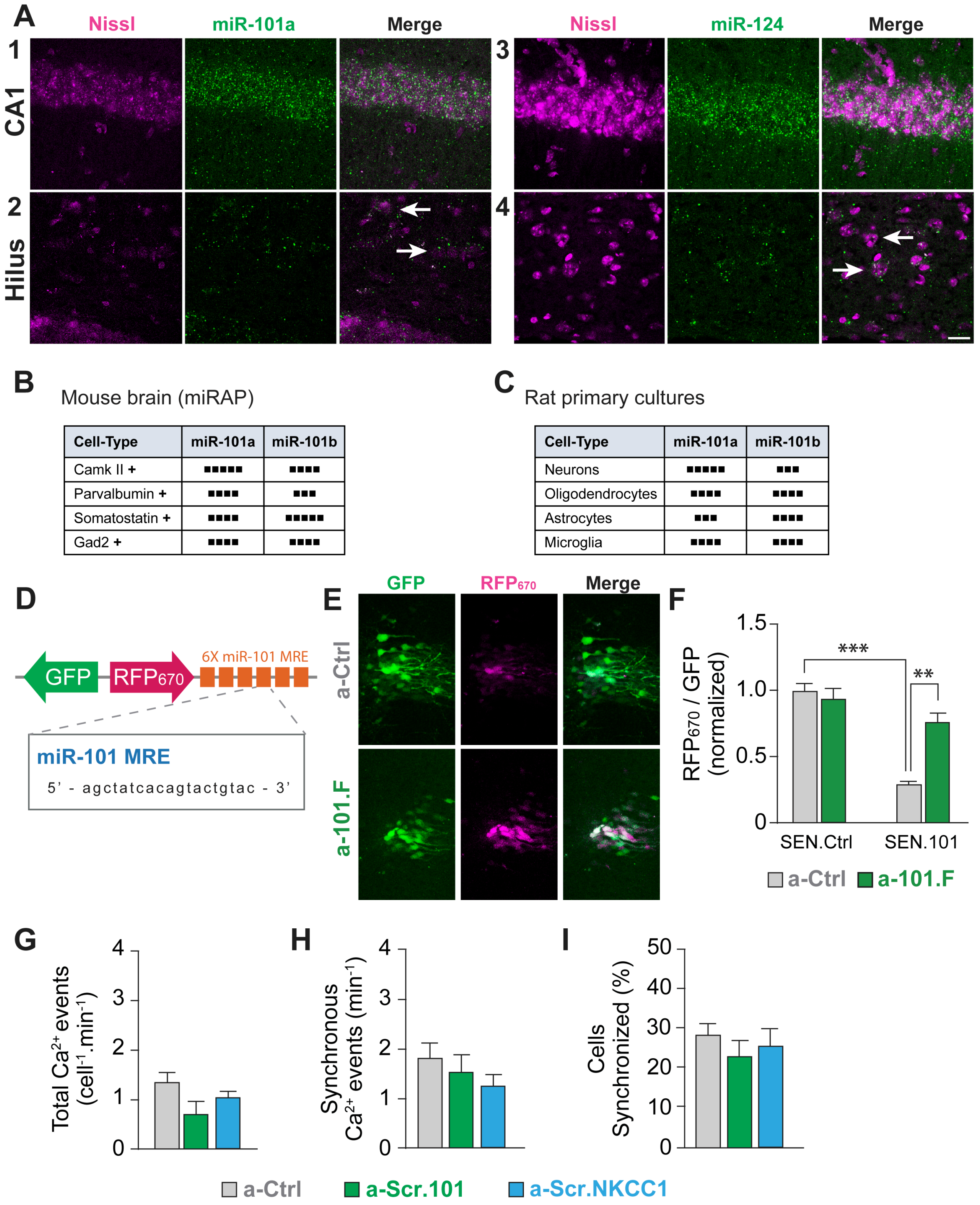

B Mouse brain (miRAP)

Cell-Type	miR-101a	miR-101b
Camk II +	■■■■■	■■■■
Parvalbumin +	■■■■	■■■
Somatostatin +	■■■■	■■■■■
Gad2 +	■■■■	■■■■

C Rat primary cultures

Cell-Type	miR-101a	miR-101b
Neurons	■■■■■	■■■
Oligodendrocytes	■■■■	■■■■
Astrocytes	■■■	■■■■
Microglia	■■■■	■■■■

Figure S2. MiR-101 is highly expressed in multiple cell-types and is efficiently blocked by a-101.F. Related to Figure 1. (A) In situ hybridization shows that miR-101 is expressed in hippocampus, both in the pyramidal layer of CA1 (1) and in the hilus (2) where interneurons, highlighted by the white arrows, are prevalent. Nissl staining (left panels) shows cell nuclei and ribosomal RNA associated with the rough endoplasmic reticulum. (3-4) Expression of miR-124, a brain enriched miR, was used for comparison. Scale bar = 20 μm. (B and C) Tables showing miR-101a and b levels in different neuronal subtypes and non-neuronal brain cells. Relative abundance is expressed on a 1-5 scale (■ =rare, ■■■■■ = very abundant). Expression levels are extrapolated from a cell-type-based analysis (He et al., 2012) performed in (B) mouse brain (miRAP) or (C) rat primary cultures (Jovicic et al. 2013). Both miR-101a and b are expressed at medium-to-high levels in all cell-types. (D to F) Sensor technology was used to demonstrate that miR-101 is present *in vivo* at high levels and can be blocked by a-101.F. (D) Top, scheme of the lentiviral construct encoding the miR-101 sensor (SEN.101). The sensor has six exactly complementary miR-101b MREs cloned downstream from RFP_{670}. Bottom, sequence of one miR-101 MRE. (E) Images of the CA1 area from animals that received the SEN.101, together with either a-Ctrl (top) or a-101.F (bottom). (F) Quantification of RFP_{670} labeling, normalized for GFP, shows that the six miR-101 MREs strongly reduce RFP_{670} fluorescence normally (in the presence of a-Ctrl) and that it is partially rescued by a-101.F. In contrast, RFP_{670} in the control sensor (SEN.Ctrl) is not reduced by expression in the cells and is unaffected by a-101.F. (G to I) Additional validation of the LNAs used. We tested two additional scrambled control oligos, one equivalent in length to the miR-101 inhibitor a-Scr.101 and the other equivalent in length to the TSB for NKCC1, a-Scr.NKCC1, with the same overall nucleotide composition. These were tested at P8 on spontaneous calcium activity compared to the original a-Ctrl and confirmed as having no effect on total calcium events (G), frequency of SEs (H), or percentage of synchronized cells (I). Bar graphs: mean ± s.e.m. One-way ANOVA. $^{**}p<0.01$; $^{***}p<0.001$.

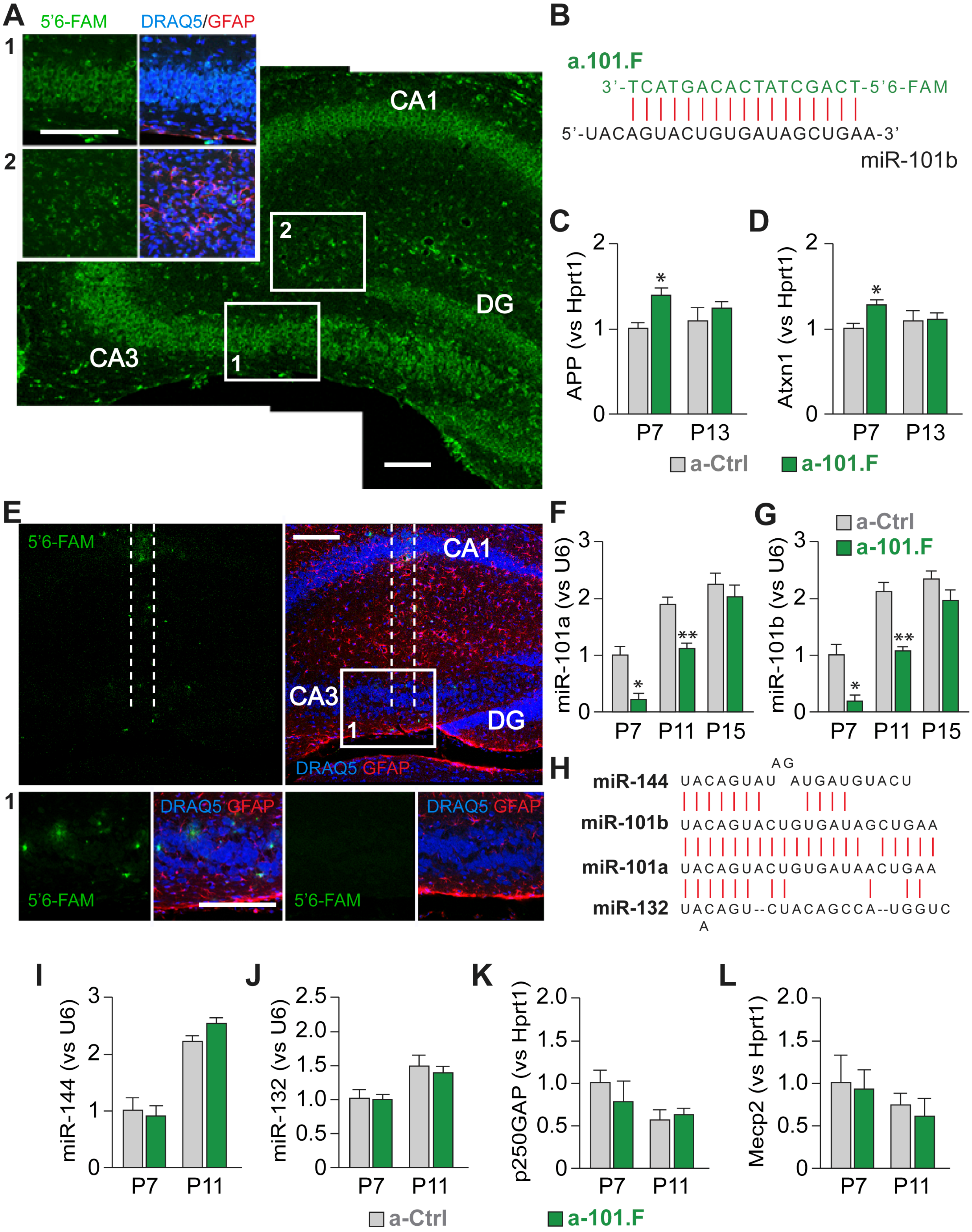
A
5'6-FAM
DRAQ5/GFAP
1
2
CA1
DG
CA3
B
a.101.F
3'-TCATGACACTATCGACT-5'6-FAM
5'-UACAGUACUGUGAUAGCUGAA-3'
miR-101b
C
APP (vs Hprt1)
2
1
0
*
P7
P13
D
Atxn1 (vs Hprt1)
2
1
0
*
P7
P13
a-Ctrl
a-101.F
E
5'6-FAM
CA1
CA3
DG
1
DRAQ5 GFAP
F
miR-101a (vs U6)
3
2
1
0
*
**
P7
P11
P15
G
a-Ctrl
a-101.F
miR-101b (vs U6)
3
2
1
0
*
**
P7
P11
P15
H
AG
miR-144 UACAGUAU AUGAUGUACU
miR-101b UACAGUACUGUGAUAGCUGAA
miR-101a UACAGUACUGUGAUAACUGAA
miR-132 UACAGU--CUACAGCCA--UGGUC
A
I
miR-144 (vs U6)
3
2
1
0
P7
P11
J
miR-132 (vs U6)
2.5
2.0
1.5
1.0
0.5
0
P7
P11
K
p250GAP (vs Hprt1)
2.0
1.5
1.0
0.5
0
P7
P11
L
Mecp2 (vs Hprt1)
2.0
1.5
1.0
0.5
0
P7
P11
a-Ctrl
a-101.F

Figure S3. Validation of miR-101 inhibition by a-101.F. Related to Figure 1. (A) High-resolution picture of a-101.F distribution in the dorsal hippocampus (CA1, CA3, and dentate gyrus (DG)), as reflected by the 5'6-FAM (a single isomer derivative of fluorescein) green tag, of a P8 animal that was injected with a-101.F at P2. The image shows that the antagonist entered the cells and accumulated in the cytoplasm during the 6-day period. Individual regions (boxes 1 and 2, lower panel) are magnified (boxes 1 and 2, upper panel). Also shown are cell nuclei (DRAQ5 staining, a far-red DNA stain, top right panel), astrocytes (GFAP immunostaining, bottom left), and the merge of all channels (bottom right). The level of a-101.F was high in the pyramidal cell layer, in astrocytes along the dorsal edge of the stratum lacunosum moleculare (box 2), and in other cell-types (most likely interneurons, glia, and endothelial cells) scattered along all strata. This is consistent with the chemistry of *in vivo*-ready LNAs that are not cell-type specific. Scale bar: 100 μm. (B) Illustration showing the complementarity of a-101.F with miR-101b (vertical red bars indicating the complementary bases) which is essential for the inhibition. The efficacy of the miR-101 inhibition is best monitored by measuring the levels of known miR-101 mRNA targets such as App and Atxn1 (Vilardo et al., 2010; Lee et al., 2008). qPCR confirmed increased levels of App (C) and Atxn1 (D) at P7 in a-101.F-treated animals versus a-Ctrl-treated animals. The inhibition subsided by P13. (E) High-resolution picture of a-101.F distribution in a P15 dorsal hippocampus, as reflected by the 5'6-FAM green tag (left) combined with DRAQ5 staining for cell nuclei and GFAP staining for astrocytes (right), after injection of a-101.F at P2. Traces of the antagonist are detected only along the needle track by this time (white dotted lines). Magnification of the indicated CA3 area (box 1 from top panel) shows clusters of extracellular a-101.F deposits and few green cell bodies (insert 1, bottom left panels). An image in the same area, but 80 μm more caudally, shows no green fluorescence though it has DRAQ5 and GFAP (insert 1, bottom right panels). Scale bar: 100 μm. (F and G) Direct qPCR of miR levels indicates that a-101.F effectively decreased miR-101a (F) and miR-101b (G) levels in the dorsal hippocampus at P7 *in vivo*. The effect is diminished at P11 and completely subsides at P15, confirming the fluorescence results above, and indicating that injection of a-101.F at P2 inhibits miR-101 transiently. (H) Illustration showing the sequence similarity (indicated by vertical red lines) among miR-101a, miR-101b, miR-144, and miR-132, particularly in the seed sequence (bases 2-8). As a result, miR-144 and miR-132 represent good candidates for assessing off-target effects of the miR-101 antagonist. Evidence for the specificity of a-101.F comes from the finding that it had no detectable off-target effects on the levels of miR-144 (I) or miR-132 (J) measured by qPCR, and no effect on the levels of two known miR-132 targets, namely p250GAP (Wayman et al., 2008) (K) and Mecp2 (Klein et al., 2007) (L), tested by qPCR. Bar graphs: mean ± s.e.m. Student’s t-test, $*p<0.05$; $**p<0.01$.

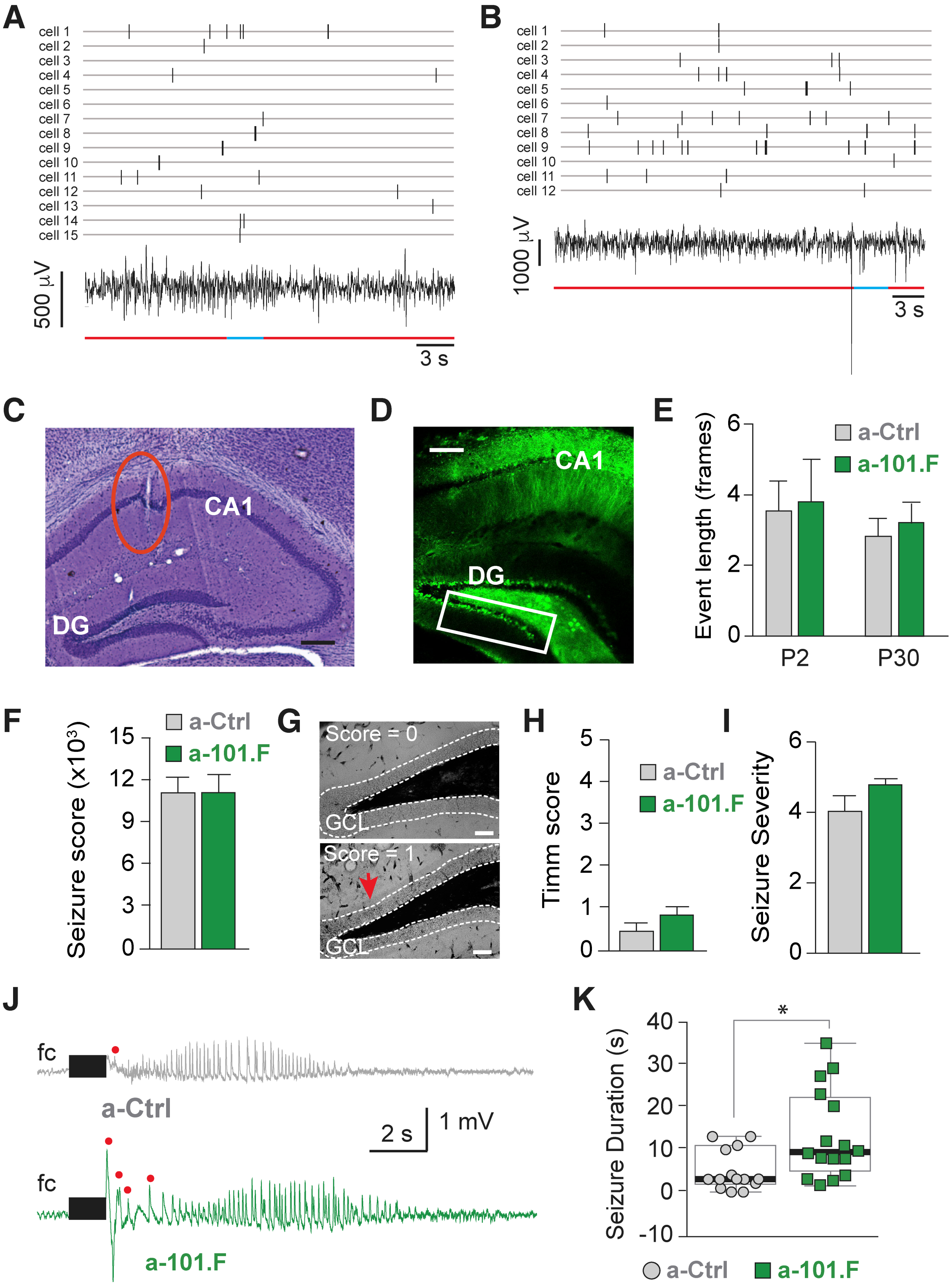

Figure S4. **Hyper-excitable network activity in a-101.F-treated young adult mice. Related to Figure 1.** (A) Action potential (spike) raster of principal cells simultaneously recorded from an a-Ctrl mouse. Each row represents the spiking activity of a single cell, with tick marks indicating spikes. The concurrent behavioral state of the animal was determined by spectral analysis of the simultaneously recorded local field potential (LFP) trace (bottom). Periods with high theta-to-delta ratios (>2) were considered 'theta' states and were removed from analysis (cyan). Periods with low theta-to-delta ratios (<2) were considered moments when the animal was quietly resting and were included in analysis (red). Spike rates reported in the main text were calculated by counting the number of spikes occurring during non-theta states, divided by seconds spent in non-theta states. (B) Recording from an a-101.F mouse, as in (A). (C) Coronal histological section stained with cresyl violet showing typical placement of tetrode in the principal cell layer of CA1 (tetrode track highlighted with red circle). Scale bars (C and D): 200 µm. (D) Representative image of P40 hippocampus after co-injection of virally encoded GCaMP6f and a-101.F at P2. Regions expressing the green GCaMP6f fluor received the miR-101 inhibitor a-101.F as well, though the latter is no longer detectable at this age. The white rectangle indicates the DG area used for analysis. (E) Average length of calcium events revealed by GCaMP6f was not changed by the a-101.F treatment at P2 (1 frame = 328 ms) or by acute injection of a-101.F at P30. (F to I) The pathological activity of a-101.F-treated mice does not represent an epileptic phenotype**.** (F) PTZ-induced seizure susceptibility in adult animals treated at P2 with a-101.F is not different from a-Ctrl-treated controls. (G and H) Mossy fiber sprouting, a hallmark of temporal lobe epilepsy, was not observed in cohorts of a-Ctrl- or a-101.F- treated animals. Example sections of Timm staining with zinc-containing fibers stained black reveal low levels of dark granules in the inner molecular layer of the dentate gyrus in both control (G, top) and a-101.F-treated animals (G, bottom). On average there was no difference in mossy fiber sprouting between controls and a-101.F-treated animals (H). (I to K) Analysis of seizures induced by MES test showed that a-101.F-treated animals had seizures with similar severity score (I) but significantly longer duration (J and K) than a-Ctrl-treated mice, indicating a network prone to pathological activity. Representative ECoG traces of seizures induced by MES test in a-Ctrl- (J, top) and a-101.F-treated (J, bottom) mice. Epidural electrodes were implanted in frontal cortex (fc). Black boxes indicate duration of electrical stimulus; red dots indicate artifacts induced by the experimenter positioning the ear electrodes. Bar graphs in (E to I) represent mean ± s.e.m.; in (K) are shown the median value (bold black line, a-Ctrl = 3, a-101.F = 9.5) and inter-quartile range (box edges). Student's t-test, except K, where Mann-Whitney U test was used; $^*p<0.05$.

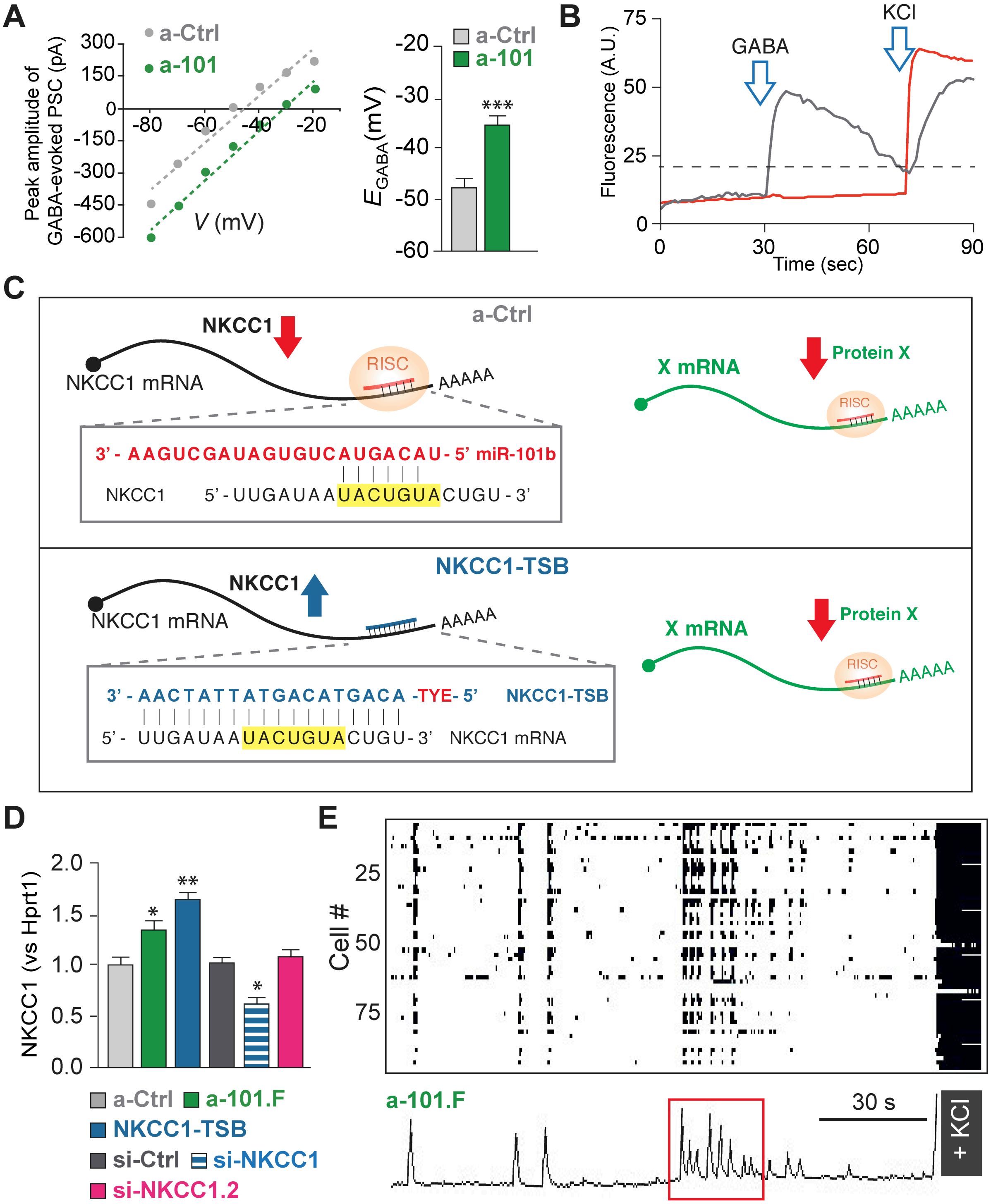

Figure S5. Effects of a-101.F and NKCC1-TSB. **Related to Figures 3, 4.** (A) Blockade of miR-101 extends the depolarizing period of GABA responses. Right, graph of mean amplitudes of hippocampal neuron responses in culture to picospritzer-applied GABA, plotted as a function of membrane potential (as done for neurons in slices in

Figure 3F-3H). Left, the extrapolated E_{GABA} values suggests that blockade of miR-101 delays the maturation of the chloride gradient, as predicted by the effects on NKCC1. (B) Traces of typical calcium transients induced by adding GABA to neurons in culture at DIV8. Grey, a neuron that responded to GABA; red, one that did not. Addition of 1M KCl was used to induce depolarization and visualize viable neurons. A dotted horizontal line represents an example of the threshold used to classify responders and non-responders. (C) Diagram showing miR-101b targeting of NKCC1 (top) and NKCC1-TSB protection (bottom). Top, miR-101b is incorporated in the RISC complex and through base-pair recognition (inset box) binds the MRE (highlighted in yellow) on the NKCC1 mRNA to induce repression (red arrow). Bottom, the NKCC1-TSB binds exclusively to the miR-101 MRE on the NKCC1 mRNA and protects it from miR-101 repression. All other miR-101 targets (X mRNA) are still repressed. The use of TSBs offers a critical advantage over manipulations used previously (e.g. over-expression of a microRNA-resistant version of the target, or direct siRNA against the target) because it does not interfere with the basal level of the mRNA. This is particularly important when the dosage of the targeted mRNA has fundamental developmental implications. (D) Injection of a-101.F at P2 increased NKCC1 mRNA levels at P8 as quantified by qPCR and normalized for the housekeeping gene Hprt1. NKCC1-TSB injected at P2 was at least as effective as a-101.F in increasing NKCC1 mRNA levels at P8. Regulation of NKCC1 by miR-101 *in vivo* had been suggested by previous work in humans (Boudreau et al., 2014). Two siRNAs against NKCC1 were also tested. While si-NKCC1 induced a significant down-regulation, si-NKCC1.2 had no effect. Because siRNAs are GapmeRs (Exiqon) and are processed by different intracellular machinery, the effect of both siRNAs on NKCC1 levels was compared to a control siRNA (si-Ctrl). (E) Selective effect of a-101.F on event frequencies. To visualize neuronal activity at P8, we loaded acute hippocampal slices with the calcium indicator Fluo-4AM and imaged calcium transients with a confocal microscope. A raster plot of population activity (upper) and principal component analysis (bottom) are shown, as in Figure 4B. A burst of spontaneous calcium transients from an a-101.F-treated mouse is indicated in the lower trace (red box). Bar graphs: mean ± s.e.m; Student's t-test. $^{*}p<0.05$; $^{**}p<0.01$, $^{***}p<0.001$.

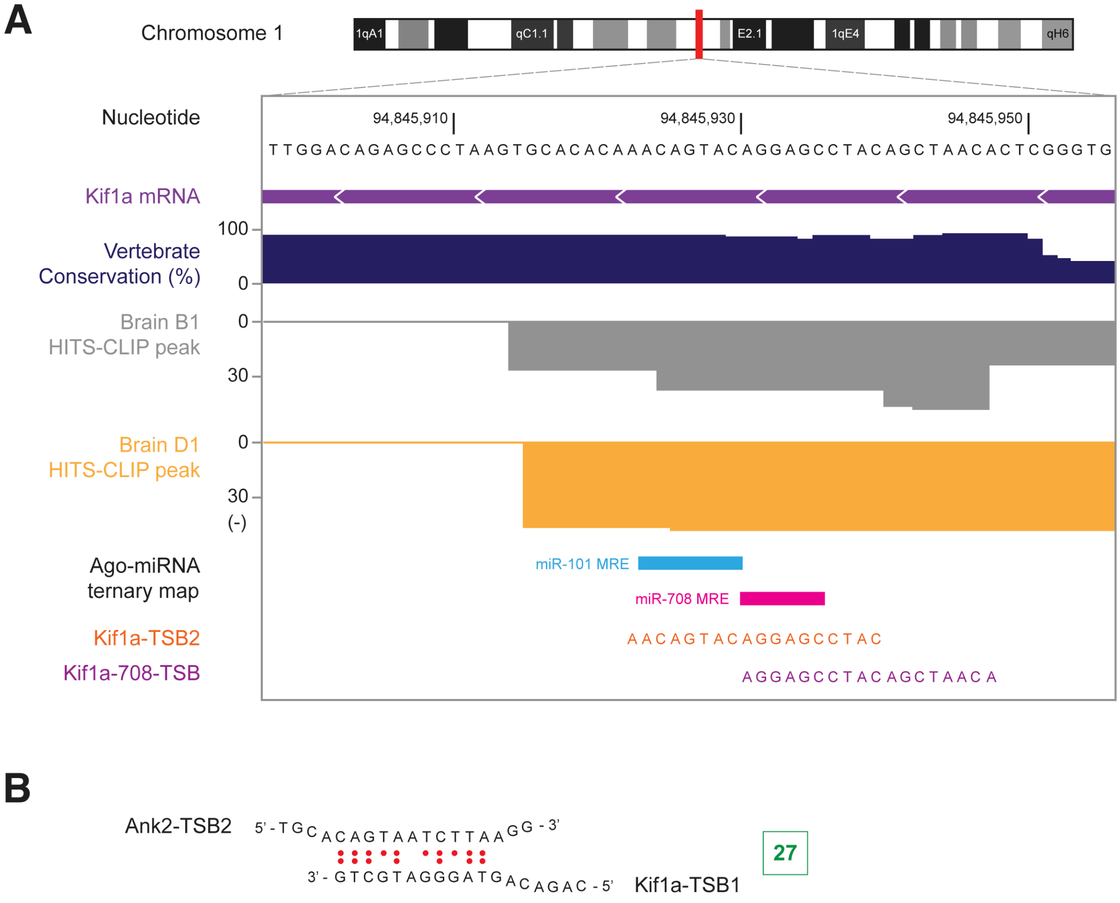

Figure S6. Example of a miR-101 recognition element and corresponding TSB. Related to Figures 4, 5. Potential targets of miR-101 were selected from an existing database derived from HITS-CLIP in the cortex at P13 (Chi et al., 2009). (A) The panel was assembled combining elements from USCS browser and Starbase. Top, scheme of mouse chromosome 1 (mm8 assembly). The red rectangle indicates the area carrying the Kif1a gene. Below the chromosome is shown a segment of the Kif1a gene sequence. The Kif1a gene is transcribed from the (-) strand as indicated by the purple bar with white arrows pointing left. The sequence including the miR-101 MRE is highly conserved (Vertebrate Conservation) and drops substantially at the end of the MRE (right part of graph). Immediately under the conservation profile and aligned to the (-) strand are shown clusters of HITS-CLIP tags used to build the Ago-miRNA ternary map shown below (Chi et al., 2009). The map was derived comparing the HITS-CLIP tags with the top predicted miRs sites. In this case the ternary map contains MREs for miR-101 and miR-708. The sequence for Kif1a-TSB2 is shown at the bottom. Kif1a-TSB2 was designed to prevent binding of miR-101 to the miR-101 recognition element in the 3’-UTR of Kif1a, thereby freeing the transcript from miR-101 inhibition. All other miR-101 targets would still be subjected to miR-101 regulation. To obtain specificity and reduce the risk of heteroduplex formation, the TSB was designed to overlap both MREs. MiR-708 is several orders of magnitude less abundant than miR-101 in the hippocampus at P12, making it unlikely to be a critical regulator. To confirm this, we designed a TSB specific for the miR-708 MRE (Kif1a-708-TSB) that would not bind to the miR-101 MRE. Injection of Kif1a-708-TSB at P2 in the dorsal hippocampus did not change the levels of Kif1a mRNA measured with qPCR (a-Ctrl = 1 ± 0.14; a-101.F = 0.88 ± 0.06; n = 3 animals). (B) Example of bioinformatics analysis performed during TSB design with the proprietary Exiqon tool (www.exiqon.com/oligo-tools). In green is the hybridization score. TSBs were designed and grouped to avoid scores >40.

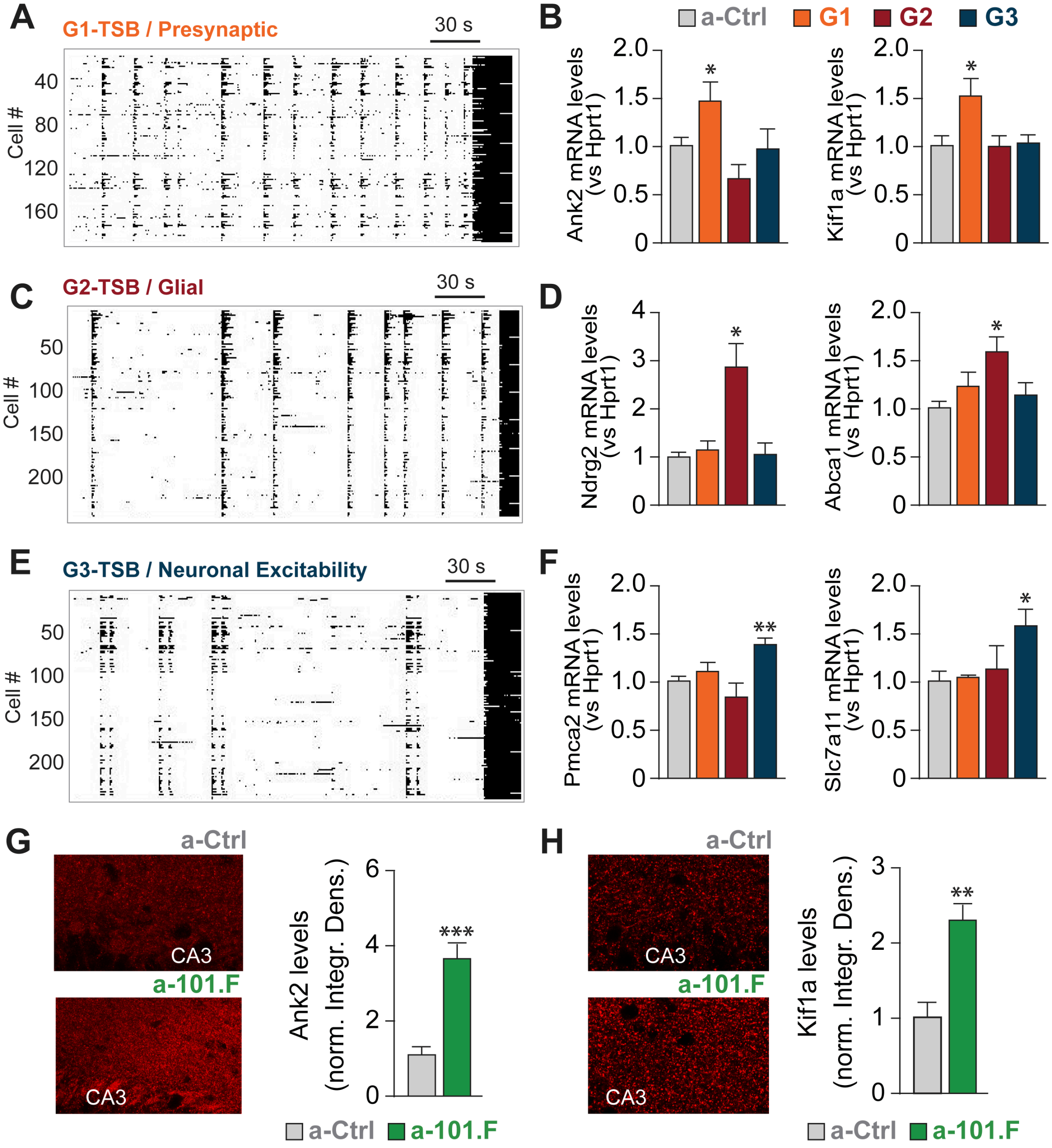

Figure S7. MiR-101 represses multiple mRNA targets to regulate spontaneous network activity. **Related to Figure 5.** (A) Raster plot of activity in a movie for Group 1 target-site blockers (G1, "Presynaptic"), which contains TSBs for Ank2 and Kif1a, along with NKCC1-TSB. Each row represents an individual cell, and each black horizontal line the duration of the calcium transients determined by how long $\Delta F/F_0$ is greater than threshold. High asynchronous activity is apparent between SEs. This is consistent with reports that Kif1a overexpression induces presynaptic boutons (Kondo et al., 2012) and that Ank2 stabilizes synapses (Bulat et al., 2014; Pielage at al., 2008).

(B) qPCR validated that G1 protected Ank2 (left) and Kif1a (right), normalized for control (a-Ctrl). In contrast, neither G2 nor G3 had an effect on either Ank2 or Kif1a. (C) Raster plot for G2 ("Glial"), which contains TSBs for Abca1 and Ndrg2, along with NKCC1-TSB. The fraction of cells participating in each event is high. This is consistent with the role of Abca1 in meeting the high lipid demand of rapidly expanding membranes during dendritic growth and synaptogenesis (Karasinska et al., 2009). (D) qPCR showed significantly increased mRNA levels for Ndrg2 (left) and Abca1 (right), while G1 and G3 had no effect. (E) Raster plot for G3 ("Neuronal Excitability"), which contains TSBs for Pmca2 and Slc7a11, along with NKCC1-TSB. A high frequency of double events is seen. This may reflect the regulation of extrasynaptic glutamate by system xCT, which is thought to promote neuronal excitability in early circuits (Blankeship et al., 2010; De Bundel et al., 2011). (F) qPCR documented an increase in mRNA levels for Pmca2 (left) and Slc7a11 (right), while G1 and G2 had no effect on these parameters. (G and H) Ank2 and Kif1a protein levels increase after miR-101 blockade. (G) Images of Ank2 immunostaining in CA3 at P8 (left). Quantification of the integrated density of the Ank2 signal (right). (H) Immunostaining analysis for Kif1a, as done for Ank2. Bar graphs: mean ± s.e.m. Student's t-test, $^{*}p<0.05$; $^{**}p<0.01$; $^{***}p<0.001$.

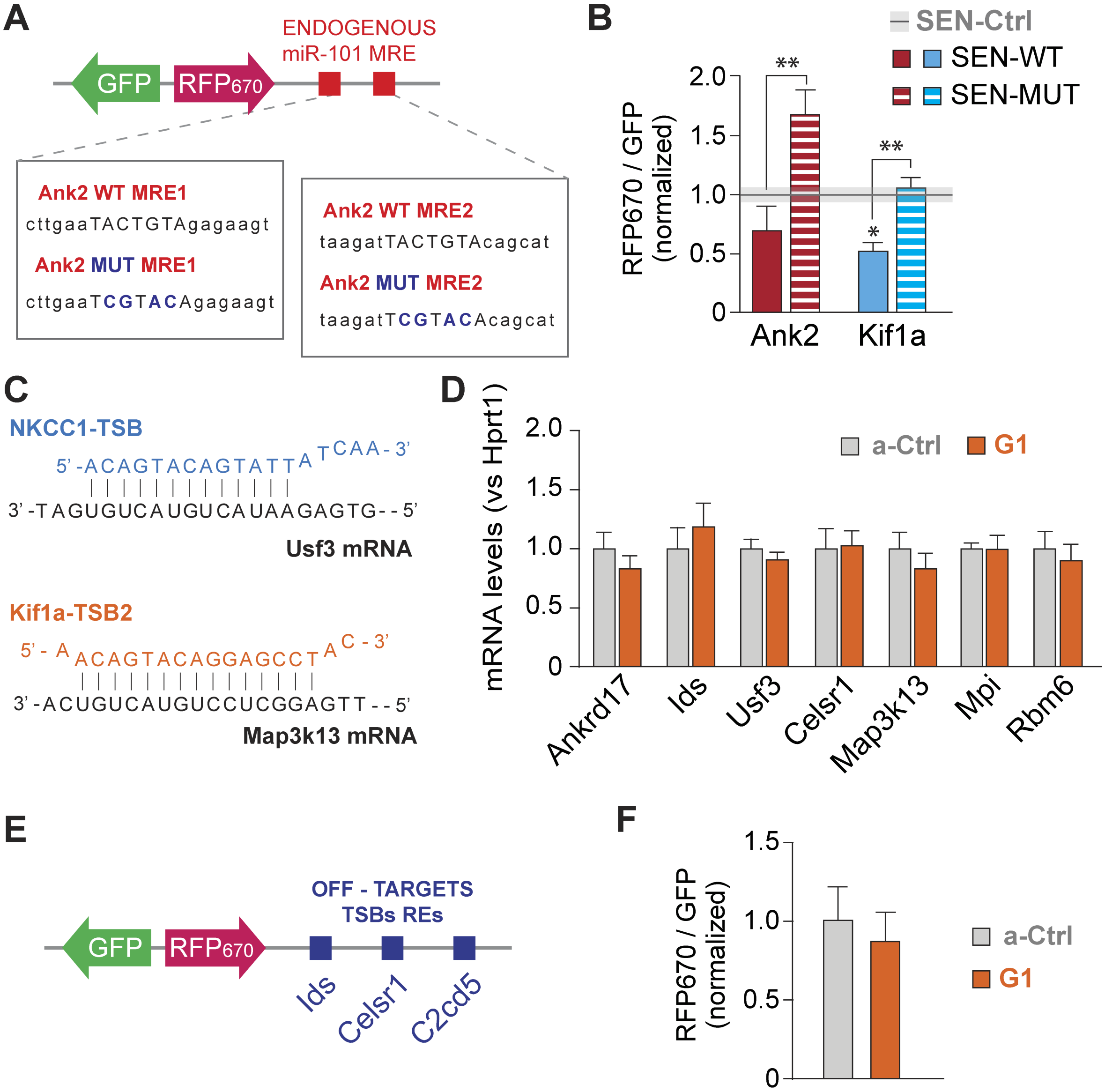

Figure S8. MiR-101 represses Ank2 and Kif1a; the TSBs are specific. **Related to Figure 5.** (A and B) Sensor technology was used to demonstrate *in vivo* that Ank2 and Kif1a are targets of miR-101. (A) Top, scheme of the lentiviral construct encoding the Ank2 sensor. Bottom, sequence of the Ank2 miR-101 MREs cloned downstream the RFP$_{670}$. (B) Quantification of RFP$_{670}$ to GFP intensity shows that mutation of the miR-101 MREs in both the Ank2 and Kif1a sensors induces an increase in RFP$_{670}$ protein levels, as it would be expected after losing miR-101 repression. Interestingly, while the Kif1a wild-type miR-101 MREs induced a significant reduction in RFP$_{670}$ compared to the control sensor, the Ank2 wild-type miR-101 MREs did not. This is likely due to a positive regulator of translation contained in the Ank2 3’-UTR. (C to F) Specificity of the TSBs. Example of possible off-target interactions between TSBs and non-specific mRNAs (C). The levels of all off-target mRNAs that showed high to moderate complementarity to the TSBs contained in G1 were tested via qPCR (D). No difference was seen at the mRNA level (E and F). Sensor technology was used to confirm at the protein level that TSBs had no off-target effects. (E) Scheme of the viral construct used for this experiment, with the off-target recognition elements from the indicated mRNAs. (F) Co-injection of G1 at P2 did not alter RFP_{670} expression at P7. Bar graphs: mean ± s.e.m. Student’s t-test except (B) One-way ANOVA. $^*p<0.05$; $^{**}p<0.01$.

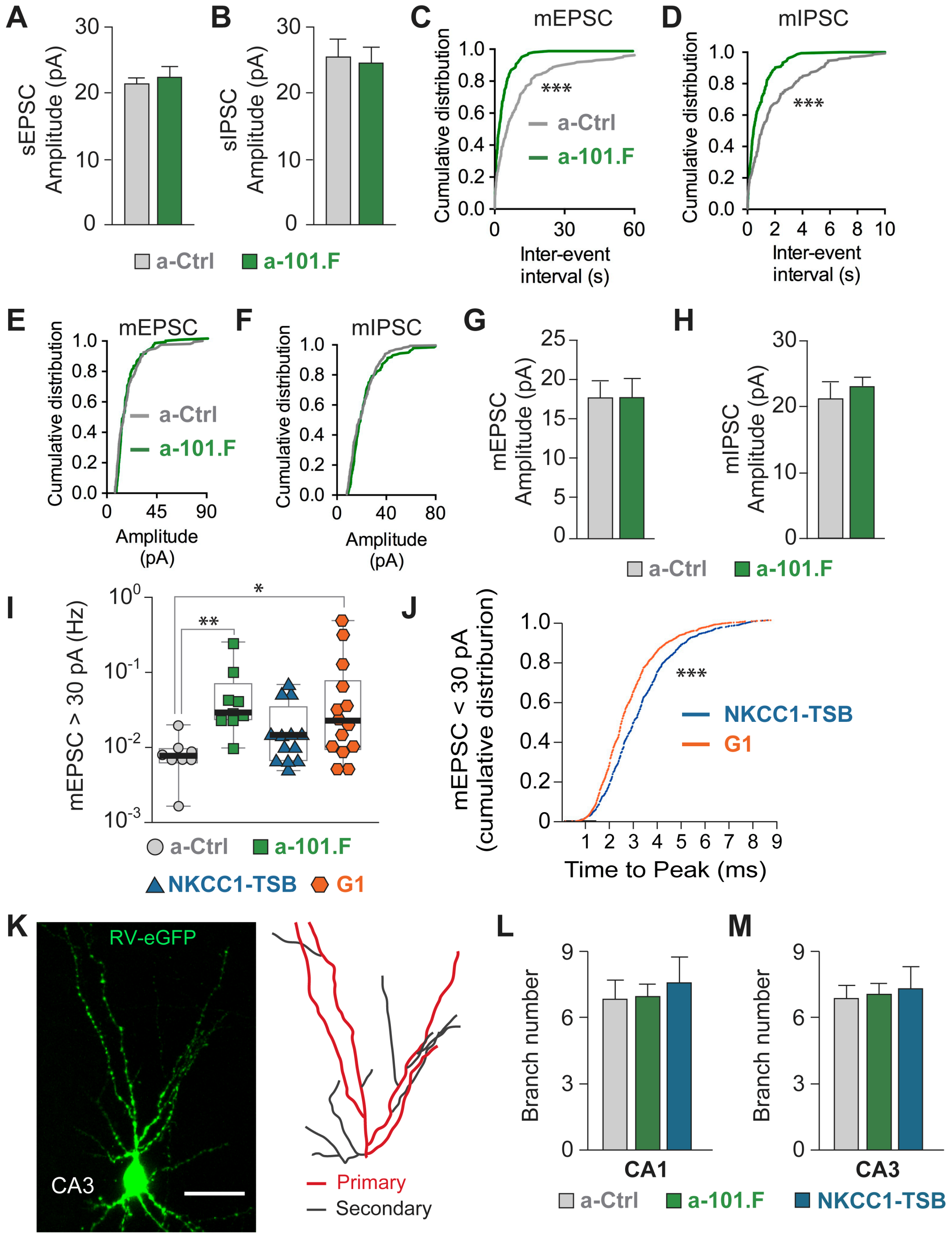

Figure S9. Effects of a-101.F vs. NKCC1-TSB and G1 on event frequencies and dendritic branches. Related to Figures 6, 7. Patch-clamp recording of synaptic events in CA3 pyramidal neurons in acute hippocampal slices from P11 mice injected with either a-101.F or a-Ctrl at P2. Mean sEPSC (A) and sIPCS (B) amplitudes. Cumulative distribution of inter-event intervals for mEPSCs (C) and mIPSCs (D) and for amplitudes of mEPSCs (E) and mIPSCs (F) in CA3 pyramidal neurons as above. Mean mEPSC (G) and mIPSC (H) amplitudes. While a-101.F did increase mEPSC and mIPSC frequencies, it did not alter event amplitude. (I) Mean frequencies of mEPSCs with an amplitude greater than 30 pA, that are more than 75% likely to be MF events. Median values, bold black line; inter-quartile range, box edges. Animals treated with a-101.F or G1 showed higher frequency of MF events, while NKCC1-TSB treatment was not different from controls. (J) Cumulative distribution of the TTP for mEPSCs with an amplitude smaller than 30 pA. Slower TTP indicates synapses that are farther away in the dendritic tree. NKCC1-TSB showed slower TTP. (K to M) Effect of miR-101 repression on dendritic complexity. Sparse labeling of CA3 hippocampal pyramidal neurons with rabies virus expressing eGFP (K, left). Scale bar: 50 μm. Characterization of dendritic morphology at P8 with NeuronJ (right). The complexity of the dendritic arborization, measured by branch number, is not affected by a-101.F or NKCC1-TSB in CA1 (L) or CA3 (M), in contrast to branch length (see Figures 7B and 7C). Bar graphs: mean ± s.e.m. Welch's t-test (A, B, G, and H). The 2 sample Kolmogorov-Smirnov test (C to F and J); Mann-Whitney U test (I). One-way ANOVA (L and M). $^{*}p<0.05$; $^{**}p<0.01$; $^{***}p<0.001$.

SUPPLEMENTAL TABLE

Gene	P11/ P7	Relative Expression (P7)					Abund.	Function
		a-Ctrl	SEM	a-101.fl	SEM	p value		
Slc12a2	0.65	1	0.04	1.46	0	0.001	■■■	Slc12a2 encodes for **NKCC1**, a chloride importer highly expressed early in development, that is partly responsible for GABA being depolarizing in young neurons (Ben-Ari, 2002). As developemnt proceeds NKCC1 levels decline, intracellular chloride levels decrease, and GABA transmission switches from being depolarizing to hyperpolarizing (Tyzio et al., 2006).
Ank2	0.69	1	0.08	1.74	0.29	0.049	■■■■	In the developing nervous system, the major isoform of **Ankyrin-2** localizes in the axon, mediates axon tract development (Scotland et al., 1998), restricts ion channels to excitable membranes by linking them to the cytoskeleton and controls synapse stability in the neuromuscular junction (Bulat et al., 2014; Pielage et al., 2008).
Kif1a	0.8	1	0.01	1.50	0.12	0.014	■■■■	The kinesin superfamily motor protein 1A (**KIF1A**) is a microtubule -based molecular motor that transports synaptic vesicle components along axons (Hirokawa et al., 2010). Kif1a overexpression induces synaptogenesis via formation of presynaptic boutons, and it is essential for enrichment-induced learning enhancement (Kondo et al., 2012).
Abca1	0.43	1	0.03	1.54	0.08	0.004	■■■	The ATP-binding cassette transporter A1 (**ABCA1**) plays a critical role in brain cholesterol metabolism. Glia-derived cholesterol is necessary to support the high lipid demand occurring during neuronal synaptogenesis (Barres et al., 2001; Jasmin et al., 2014). ABCA1 ablation in the CNS results in multiple synaptic deficits (Karasinska et al., 2009).
Ndrg2	0.49	1	0.06	1.40	0.13	0.046	■■■■■	**Ndrg2** belongs to the family of N-myc downregulated genes. Ndrg2 is highly expressed in neurogenic germinal zones during development (Liu et al., 2012) where it is thought to suppress proliferation and stabilize morphology (Takeichi et al., 2011). In postnatal brain it is mostly expressed in the subgranular zone of the DG (Liu et al., 2012) and in glia. Ndrg2-postive glial processes are associated with VGLUT1 and VGAT terminals suggesting a role at the synapse (Flügge et al., 2014).
Slc7a11	0.59	1	0.07	1.97	0.40	0.046	■■■	Slc7a11 encodes system **xCT,** which exchanges intracellular glutamate for extracellular cysteine (Bannai et al., 1986), thereby raising the concentration of extrasynaptic glutamate. System xCT knockout mice show impaired spatial working memory and have a higher threshold for pilocarpine-induced limbic seizures (De Bundel et al., 2011) suggesting that xCT levels play a key role in hippocampal circuit formation. Before synaptic structures are mature, extrasynaptic glutamate plays an important role in propagating waves of depolarization (Demarque et al., 2002). In addition, it depolarizes interneurons via NMDA receptors to increase the frequency of SE, and it activates extrasynaptic NMDA receptors to enhance cell excitability and convert silent synapses to functional status (Cattani et al., 2007; Durand et al., 1996).
PMCA2	0.8	1	0.19	1.7177	0.3	0.040	■■■■	The plasma membrane Ca2+ ATPase (**PMCA**) is part of the Ca2+ regulatory system in neurons (Brini et al., 2013) and helps return intracellular Ca2+ to basal levels (Benham et al., 1992). PMCA2 regulates a variety of Ca2+ signaling processes including neurotransmitter release (Empson et al., 2007; Zenisek et al., 2000) and synaptic plasticity (Gomez-Varela et al., 2012).
Rapgef1	0.47	1	0.05	1.42	0.08	0.010	■■■■	
Slc25a4	0.72	1	0.09	1.03	0.08	0.135	■■■■	
Camk2a	1.07	1	0.13	1.23	0.17	0.881	■■■■	
Clasp2	0.55	1	0.13	1.20	0.13	0.339	■■■■	
Dbs	0.65	1	0.07	0.98	0.07	0.888	■■■	

Table S1. List of miR-101 candidate targets. **Related to Figures 3, 4, and 5.** Shown are the top 12 mRNA targets (out of 17 tested). The first 7 were selected for analysis. qPCR was used to compare mRNA levels at P7 and P11 to determine which candidates showed a developmental decrease consistent with the miR-101 increase. Data were normalized to P7 values (P11/P7). Next, mRNA levels were tested when miR-101 was blocked by a-101.F. Values are expressed as mean ± s.e.m., normalized for values seen in a-Ctrl-treated control mice, with p values from Student's t test (Relative Expression (P7)). The relative abundance of tested mRNAs (Abund.) was extrapolated from qPCR C_T values and expressed on a 1-5 scale (■ =rare, ■■■■■ = very abundant). The functions of the encoded proteins are summarized, focusing on their roles in development and neurodevelopmental disorders (Function). The targets are listed according to TSB grouping and are not ranked by importance.

SUPPLEMENTAL EXPERIMENTAL PROCEDURES

Animals

Animal experiments and ex vivo experiments were conducted at the University of California at San Diego (UCSD) and at the University of Modena and Reggio Emilia (UNIMORE). To ensure reproducibility and consistency of results, all animals (C57Bl/6J, RRID:IMSR_JAX:000664) were purchased from the same provider (Harlan Laboratories), all locked nucleic acid (LNA) reagents were purchased from the same manufacturer (Exiqon), and aliquots came from the same batch.

Animals were housed under 12/12 h light/dark cycle (07:00 AM-7:00 PM) at 23 ± 1°C with free access to food and water. All experimental procedures at UCSD were performed as approved by the Institutional Animal Care and Use Committee and according to the National Institutes of Health Guidelines for the Care and Use of Laboratory Animals. Behavioral and *in vivo* experiments at UNIMORE were conducted in accordance with the European Community Council Directive (86/609/EEC) of November 24, 1986, and approved by the ethics committee.

Small RNA sequencing

MicroRNA analysis was performed in collaboration with the Yeo lab at UCSD as described (Zisoulis et al., 2010). Total RNA was extracted from both hippocampi of 6 P12 C57BL/6J male mice using the miRNeasy mini kit (Qiagen). The sequencing pipeline is based on the Illumina's Small RNA Digital Gene Expression v1.5 protocol with minor modifications to include indexing and multiplexing of RNA samples. Small RNA reads were mapped to the mouse mm9 genome using Bowtie aligner (m=20, n=1, l=18, --best; RRID:SCR_005476) and then to UCSC smRNA and mirBase16 annotations (18 bp minimum; RRID:SCR_003152) to assign miR identity. Lastly, to account for differences in amplification efficiency due to barcoding, the reads for each miR were expressed as percentage of the total reads for that sample and the percentage averaged across the 6 animals to produce the pie shown in Figure S1A.

Semi-quantitative PCR (qPCR)

qPCR was used to measure levels of both miRs and their mRNA targets. The small nuclear RNAs U6 and sno234 were used as housekeeping genes for normalization of miR qPCR, while Hprt1 was used as housekeeping gene for normalization of mRNA qPCR. Total RNA was extracted from dorsal hippocampus or acute hippocampal slices as previously described (Lippi et al., 2011) using miRNeasy mini kit (Qiagen). Briefly, animals were decapitated and the brain dissected on an ice pad. The dorsal hippocampus was isolated, immersed in Qiazol (Qiagen), and immediately homogenized with a syringe and 23-gauge needle. RNA extraction was performed following manufacturer's instructions. Levels of miRs were assessed using TaqMan microRNA assays (Applied Biosystems) following manufacturer's recommendations. For reverse transcription, sequence-specific primers were added for each miR being tested and for housekeeping genes U6 and sno234. Real-Time PCR analysis was conducted on a Light Cycler 480 system (Roche), and the data were processed and analyzed using the comparative Δ_{CT} method (Livak et al., 2001). Levels of miR-target mRNAs were assessed with Universal Probe Library (UPL) Taqman Assays (Roche), following manufacturer's recommendations. Reverse transcription was performed as previously described (Ziviani et al., 2010). Each qPCR experiment used 3-6 animals per condition. Primers for each assay were designed using the Roche online tool (Assay Design Center). Below is a list of the primers used and their respective UPL probe. For the housekeeping gene Hprt1, we used two sets of primers with slightly different amplification efficiency. This allowed optimal matching with the primer sets for the experimental genes.

MiR-132 known targets:

p250GAP. Forward: gcccttacctggatggagat; Reverse: cttgataacatgggcagcac; Probe: 18.

Mecp2. For: tctgaaggactgggaggtgt; Rev: gccttaatcactggccaact; Probe: 2.

MiR-101 known targets:

App. For: cgagagagaatgtcccaggt; Rev: cttcctgttccagagattcca; Probe: 2.

Atxn1. For: tttttgcaccttattgaaaagaaac; Rev: gagagtatgcacgcatatggaa; Probe: 2.

MiR-101 potential targets:

NKCC1. For: gctaccaatgggttcgtgag; Rev: aaattccggccctagacttc; Probe: 101.

Ank2. For: ccaggagccagttcaacaag; Rev: tctgcccctggtgttgttac; Probe: 18.

Kif1a. For: tgggacagttccatgcataa; Rev: ctggctgggtacagttctcc; Probe: 18.

Abca1. For: ttccatcctccttgtcatctc; Rev: tccttggcaaagttcacaaa; Probe: 89.

Ndrg2. For: tacttcctgcaaggcatgg; Rev: ctcgctactctgcgacagg; Probe: 89.

Rapgef1. For: acccagttcacagagcacttc; Rev: tcttgatgaacttgaggagcag; Probe: 2.

Slc7a11. For: cagtggggcaccaatctataa; Rev: ggtcccaaatagtcaatgctg; Probe: 89.

Pmca2. For: tggcatcatatttaccctgct; Rev: tcagaggctgcatctccat; Probe: 18.

Camk2a. For: gagtggcccctagttctgg; Rev: aggcaggcgaggctttag; Probe: 89.

Dbs. For: ccttggagctgcatagcc; Rev: tgggactggcatttgtcc; Probe: 18.

Slc25a4. For: gagctgcctacttcggagtct; Rev: gggcaatcatccagctca; Probe: 89.

Clasp2. For: gaaatgccaagaccgactct; Rev: aactcttcctggagacccaga; Probe: 7.

Gria2. For: ttttcttggaaatgcaaaagatt; Rev: agcgccccttggaaatag; Probe: 2.

Off-target TSB genes:

Ankrd17. For: tccatgttcatcagcatcaaa; Rev: gtgcacgaactccagaggat; Probe: 67.

Ids. For: ctcggattggatggatgc; Rev: caacatgaaaagaagggatgg; Probe: 101.

Usf3. For: ctgtgttctgcccctgct; Rev: gagccccacaggagctactaa; Probe: 2.

Celsr1. For: aagccctcagaccttgaagc; Rev: ctcacacaaggtgcctgct; Probe: 95.

Map3k13. For: ctgagtcccacggattgg; Rev: ctgaggcagtcacagaagca; Probe: 18.

Mpi. For: tccagggcttgtgtggtt; Rev: actggaactcaggcaccttc; Probe: 25.

Rbm6. For: gggaagcctcccctagaag; Rev: acccaggagaccaatcagtg; Probe: 101. .

Housekeeping gene:

Hprt1. For: ggagcggtagcacctcct; Rev: ctggttcatcatcgctaatcac; Probe: 101.

Hprt1. For: cctcctcagaccgcttttt; Rev: aacctggttcatcatcgctaa; Probe: 95.

Bio-informatics tools

MiR-101 HITS-CLIP targets analysis with DAVID. The list of miR-101 targets was obtained from the "Ago-miRNA-mRNA ternary map by HITS-CLIP" website hosted by the Darnell lab (http://ago.rockefeller.edu/tag_mm9.php). The full Ago ternary map table (mm9) was downloaded, and the miR-101 targets were selected. The list of 734 Ago-miRNA-mRNA complexes attributed to miR-101 was then loaded into the online functional annotation tool DAVID (Huang et al., 2009) (RRID:SCR_001881; david.abcc.ncifcrf.gov/) using GOTERM BP FAT. The list in Figure S1D shows the top 13 biological themes ranked by false discovery rate (FDR, second column) followed by 6 out of the top 30 that were particularly interesting for development. FDR is the rate of type I errors in experiments with null hypothesis when multiple comparisons are necessary. FDR indicates the expected proportion of "discoveries" (rejected null hypotheses) that were false (incorrect rejections). An important criterion for selection was the enrichment that represents how relevant a biological theme is in the subset of genes being analyzed. The enrichment was calculated by comparing the percentage of genes from the list of miR-101 HITS-CLIP targets that belong to a given biological theme compared to the population background (the percentage of genes belonging to the same biological theme in the entire mouse genome). The p value (left column) is derived with a modified Fisher's exact test (EASE score) and is an indication that the specific biological theme is significantly more enriched than random chance (for more details see Huang et al., 2009).

Starbase. To narrow down the number of miR-101 HITS-CLIP targets, we used Starbase (Yang et al. 2011) (starbase.sysu.edu.cn/), a tool designed to decode interaction networks of non-coding RNAs and mRNAs, and traditional miR prediction software such as Targetscan (RRID:SCR_010845; www.targetscam.org), RNA22 (http://cbcsrv.watson.ibm.com/rna22.html), and PicTar (http://pictar.mdc-berlin.de/).

Injections of LNAs and virus

P2 injections. Surgeries were performed under sterile conditions. General anesthesia was induced in P2 neonates with deep hypothermia alone as described (Lozada et al., 2012). Briefly, the pups were placed on crushed ice covered with Saran wrap to avoid freeze damage to the skin. Injections were performed with a Nanoject (Lozada et al., 2012) (Drummond Scientific Company, Broomall, PA) and a beveled glass injection pipette (Adesnik et al., 2008). Animals received two injections in each dorsal hippocampus (see Figure 1A for an illustration of the procedure). The glass pipette (Flared Glass: 4.45 cm long, 90 μm diameter) was lowered 2 mm below the skull level and then retracted 1 mm; 207 nl were injected for each site. After surgery, pups were placed on a heated pad for few min until they were warm and capable of spontaneous movement. All vestiges of blood were gently removed from the pups to minimize chances of the dam rejecting the pups.

The concentration for LNA injection was extrapolated from previous work (Hollander at al., 2010; Jimenez-Mateos et al., 2012; Zovoilis et al., 2011) and adjusted for miR abundance and volume of the dorsal hippocampus at P2. Concentrations used were 0.5-1 μM for a-101.F and a-Ctrl (Exiqon), 165-333 nM each for the TSBs (Exiqon). For rescue experiments, 0.5 μM a-101.F was mixed with 0.2 μM GapmeR siRNAs (Exiqon) .

The LNAs injected had the following sequences:

Antagonists:

a-Ctrl: gtgtaacacgtctatacgccca.

a-Scr.101: attctagcgcataactc.

a-Scr.NKCC1: atcatatacgactagtaa.

a-101.F: tcagctatcacagtact.

Target site blockers:

NKCC1-TSB: acagtacagtattatcaa.

Kif1a-TSB1: cagacagtagggatgctg. Kif1a-TSB2: aacagtacaggagcctac.

Ank2-TSB1: tcacagtattcaagtttt. Ank2-TSB2: tgcacagtaatcttaagg.

Abca1-TSB1: tacagtatccagtttgtt. Abca1-TSB2: tacagttctaagcttcca.

Abca1-TSB3: tacagtagtttgaggttt.

Ndrg2-TSB: acgtcacagtatggtcag.

Slc7a11-TSB1: cacagtaagaattacatg. Slc7a11-TSB2: ttcacagtatagatgtcc.

Pmca2-TSB1: tcccacagtagtgacatt. Pmca2-TSB2: aaaggctacagtatata.

Pmca2-TSB3: tacagtgagttctgacaa.

Kif1a-708TSB: aggagcctacagctaaca.

GapmeRs (siRNA):

si-Ank2.1: gaaaacaactggcgta.

si-Ank2.2: caatttggctagtggt.

si-Kif1a.1: ggttgacaatagtggt.

si-Kif1a.2: aaggaggcattcggac.

si-NKCC1: attggagcaataacgt.

si-NKCC1.2: tacgatgcaaggaaga.

si-Ctrl: aacacgtctatacgc.

For the calcium imaging experiments in P40 mice, 5 mM LNAs were mixed at room temperature with GCaMP6f adeno-associated viral particles (UPenn viral core, AAV1.Syn.GCaMP6f.WPRE.SV40) at a 1:10 ratio before the injection. Male mice were injected at P2 as described, weaned at 4 weeks of age, and housed up to 6 per cage.

For the analysis of dendritic structure at P8 and dendritic protrusions at P11, a glycoprotein-deleted variant of the SAD-B19 strain of rabies virus encoding eGFP (SAD Δ G-eGFP) was mixed with LNA antagonists at a 1:10

ratio. Such a low titer was necessary to achieve sparse labeling of both CA1 and CA3 pyramidal neurons. The virus was kindly provided by Byungkook Lim.

P30 stereotaxic injections. P30-32 animals were anesthetized with ketamine (100 mg/kg)/xylazine (10 mg/kg), and placed in the stereotaxic apparatus. LNAs (a-101.F or a-Ctrl) were combined with AAV1.Syn.GCaMP6f.WPRE.SV40 for a total concentration of 500 nM LNAs. Approximately 850 nl of the viral/LNA mixture was infused into each hemisphere, targeting the dorsal hippocampus using the following coordinates, from bregma: AP: -1.9 mm, ML: 1.0 mm, DV: -2.1 mm. Injections were performed with a Nanoject II and pulled glass pipettes, at a rate of 120 nl/min. The pipette was left in place 5 min before removal. Animals were placed on a Deltaphase® isothermal pad to recover and subsequently returned to their home cages.

***In Vivo* Single Unit Recording**

Surgery. At 90 days of age mice were implanted with a microdrive recording device (a-Ctrl, n = 5 animals, 26 cells; a-101.F, n = 7 animals, 20 cells). Mice were anesthetized with isoflurane (2 – 2.5% in O_2), and an electrode assembly that consisted of 4 tetrodes (bound together) was implanted above the right hippocampus (AP, 1.8 mm posterior to bregma; ML, 1.8 mm) and fixed to the skull using stainless steel screws and dental cement. One screw was used as animal ground and was implanted to touch the surface of the brain above the cerebellum. Tetrodes were prepared by twisting 4 insulated platinum wires (diameter = 0.017 mm, California Fine Wire Company) together and melting the insulation to bind the four electrodes. Electrodes were plated with platinum prior to surgery to have stable impedances near 200 MΩ. Animals were given one week to recover from surgery.

Local field potential (LFP) video monitoring and single unit recording. In each mouse the chronically implanted electrode was connected to a unity-gain operational amplifier. The output of the preamplifier was conducted via a lightweight multi-wire tether to a data acquisition system (Digital Lynx SX, Neuralynx) with 32 digitally programmable amplifiers. Unit activity was amplified and band-pass filtered between 0.6 and 6 kHz. Spike waveforms above a trigger threshold (40 μV) were time-stamped and digitized at 32 kHz for 1 ms. The LFP was recorded continuously in the 0.1-900 Hz band from one of the wires of each tetrode. Over several days the tetrode bundle was advanced to the pyramidal cell layer (CA1 and CA3 were pooled). Once the tetrodes were placed in the cell layer, LFPs and videos were recorded for 4 h to determine whether ictal or inter-ictal activity was present. Single units were recorded in 6 out of 7 a-101.F mice and in 3 out of 5 a-Ctrl mice. After recording in the cell layer, tetrodes were advanced to the hippocampal fissure, and LFPs and videos were recorded for an additional 4 h. All recordings were obtained while animals were resting in their home cages.

Detection of seizures and inter-ictal spikes. LFP traces were visually scanned for seizures and inter-ictal spikes off-line, and possible seizure start times were noted. Next, the corresponding video was observed to determine whether the suspected period was associated with a stage III, IV, or V seizure on the Racine scale (Racine, 1972). Inter-ictal spikes and two stage III seizure events were recorded in 1 out of 7 a-101.F mice. No other animal (including controls) had seizures or inter-ictal spikes.

Single unit isolation and analysis. For each recording with single units, a period of 20 min was selected for manual sorting using MClust (MClust 3.5, written by A. David Redish; http://redishlab.neuroscience.umn.edu/MClust/MClust.html) as reported (Mankin et al., 2012). For each recording session, the tetrode with the largest theta (5-11 Hz) to delta (2-4 Hz) (θ / δ) power ratio was selected by performing spectral analysis of the LFP using the Chronux package (www.chronux.org). Next, the θ / δ ratio of the signal on the selected tetrode was calculated for each 3-s bin of the recording session. Bins that had $\theta / \delta < 2$ were scored as non-theta periods, and bins that had $\theta / \delta > 2$ were scored as theta periods (Ewell et al., 2015). Single units were excluded from analysis if they were not separable from either the noise or other single units. Spike rates reported in the manuscript were calculated for non-theta bins and averaged.

Histology and reconstruction of electrode tracks. Once electrophysiological experiments were concluded, all mice received an overdose of sodium pentobarbital, and were perfused intracardially with 1X phosphate buffer solution (PBS) followed by 4% paraformaldehyde (PFA) in PBS. Brains were extracted and stored overnight in the PFA solution, then transferred to 30% sucrose in PBS until sectioned with a freezing microtome. Forty μm thick coronal sections were cut through the segment of the hippocampus with electrode tracks, and each section was stained with cresyl violet. The tetrode positions were determined by reconstructing the positions of all tetrodes across serial sections. A small angular deviation between the plane of sectioning and the electrode tracks resulted in an apparent shift of the tissue damage between sections (Leutgeb et al., 2005). The electrode tip was considered to be located in the section where the tissue damage was most posterior.

Timm staining

Mice were perfused intracardially with 0.37% sodium sulphide solution (pH 7.2) followed by 4% PFA in a PBS (0.1M sodium phosphate, pH 7.3 - 7.4). Brains were extracted, post-fixed in 4% PFA overnight, and then transferred to 30% sucrose in PBS. Brains were frozen, sectioned (40 μm) with a microtome, and mounted. Mounted slices were washed in distilled water, incubated in developer solution (consisting of 50% gum arabic, 25.5% citric acid and 23.5% sodium citrate aqueous solution, 1.7% hydroquinone, and 0.09% silver nitrate solution) within a light-free container, washed again in warm and distilled water in another light-free container, and fixed in sodium thiosulfate pentahydrate, dehydrated in ethanol, and cover-slipped. Synaptic reorganization of mossy fibers within the supra-granular region of the dorsal dentate gyrus was scored on a scale of 0 – 5, adapted from previous work (Cavazos et al., 1991). Timm staining was carried out on 3-6-month-old adult male mice littermates (from 7 litters) for a-Ctrl and a-101.F (n = 5, 10, respectively).

Pentylenetrazole infusion test

Seizure susceptibility was tested with a single subcutaneous injection of pentylenetetrazole (PTZ, 0.5 mg/kg) as shown before (Ganor et al., 2014), with slight modifications. Mice were injected, immediately placed in clear plastic cages (15x20x20 cm), and carefully observed for 30 min. PTZ-induced seizure activity was quantified according to the following scale (as shown in Ganor et al., 2014; adapted from Ferraro et al., 1999): (1) Hypoactivity: progressive decrease in motor activity until the animal becomes immobile in a crouched or prone position, with abdomen in full contact with the bottom of the cage. (2) Partial clonus: clonic seizure activity affecting face, head, and/or forelimbs. Partial or focal seizures are brief, typically lasting for 1-2 s, often accompanied by vocalizations. (3) Generalized clonus: sudden loss of upright posture, whole body clonus involving all four limbs and tail, and rearing. (4) Tonic-clonic (maximal) seizure: generalized seizure characterized by tonic hindlimb extension. Latencies to hypoactivity (HA), partial clonus (PC), generalized clonus (GC), and maximal tonic-clonic (TC) behavioral seizures were recorded. The seizure severity was calculated with a quantitative seizure score, according to the following equation: seizure score = 0.1 x (1/HA latency) + 0.2 x (1/PC latency) + 0.3 x (1/GC latency) + 0.4 x (1/TC latency). The cage was accurately wiped with 70% ethanol after each test to avoid olfactory cues. For PTZ infusion test n = 20 and n = 22 adult mice were tested for a-Ctrl and a-101.F respectively.

In vivo MES test

Electrode implantation for electrocorticogram (ECoG) recordings. After deep anesthesia (ketamine-xylazine, 150-10 μg/g), the skin was shaved, disinfected (10% povidone-iodine, Betadine® skin solution Meda Pharma, Milano, Italy), and opened to expose scalp. Guiding holes were drilled, and epidural electrodes (stainless steel Ø = 1 mm; PlasticsOne, Roanoke, VA, USA) were implanted in frontal (bregma 0 mm, 3 mm lateral from midline) and occipital cortices (bregma -3.5 mm, 3 mm lateral from midline) of left hemisphere. A reference electrode was implanted below lambda in the midline. Electrodes were connected by steel wire to terminal gold pins (Bilaney Consultant GmbH, Düsseldorf, Germany) that were inserted in a plastic pedestal (PlasticsOne) cemented on the mouse head. To reduce pain and risk of infection, after surgery we applied a gel containing 2.5 g lidocaine chloride, 0.5 g neomycin sulfate, and 0.025 g fluocinolone acetonide (Neuflan® gel; Molteni Farmaceutici, Scandicci, FI, Italy). Mice were kept under heat lamp and monitored until complete recovery from anesthesia; they were then housed in single cages without grids or environmental enrichments to reduce risk of headset lost.

Video-ECoG recordings. Mice were placed in cages without cover to allow cable connection between headset and preamplifiers. Electrical brain activity was filtered (0.3 Hz high-pass, 500 Hz low-pass), acquired at 1 kHz per channel, and stored on a computer. Traces from the reference electrodes were subtracted from the recording electrodes traces, using a PowerLab8/30 amplifier connected to 4 BioAmp preamplifiers (ADInstruments; Dunedin, Otago, New Zealand). Videos were captured by a camera connected to the computer and synchronized to the ECoG traces by LabChart 7 Pro internal trigger.

MES test. Mice 3- and 9-months-old were analyzed, after having received either a-Ctrl (n = 5, 10 for 3- and 9-months-old, respectively) or a-101.F (n = 8 for each age). No age-related differences were observed in any parameter, so data were pooled for the analyses. A mouse alone in a cage was connected to the ECoG recording system and given a current stimulus (100 Hz, pulse width 0.5 ms, shock duration 0.7 s, current amplitude 10 mA) via ear-clip electrodes connected to an ECT unit (Mares et al., 2006) (model 5780, Ugo Basile, Comerio, Italy). Ear electrodes were soaked in 0.9% saline immediately before use. During stimulation, ear-clips were held by the experimenter and released immediately afterwards. Seizures were video-ECoG recorded. Artifacts in ECoG traces due to experimenter presence are indicated.

ECoG analysis. ECoG traces were digitally filtered offline (band-pass: high 50 Hz, low 1 Hz) and manually analyzed using LabChart 7 Pro software (AD Instruments). Seizures were characterized by epileptiform ECoG patterns with trains of 150-250 ms long spikes. No spontaneous seizures or inter-ictal activity was detected in a-

101.F- or a-Ctrl-treated animals during a 4 h (2 h in the light, 2h in the dark) baseline ECoG recording, before the MES test.

Behavioral analysis. Videos containing current-induced responses in mice were analyzed offline. Severity of seizures was graded according to the following scale: 0: no response; 1: facial muscle twitching; 2: head nodding; 3: clonus, jumps, wild running; 4: straub tail; 5: tonic-clonic seizures; 6: respiratory arrest and death (Mares et al., 2006).

Electrophysiology of hippocampal slices

Slice preparation. Male mice were decapitated after anesthesia with 1 mg ketamine + 100 μg xylazine/g body weight. Brains were quickly removed and placed in an ice-cold solution containing (in mM): 75 sucrose, 87 NaCl, 2.5 KCl, 0.5 $CaCl_2$, 7 $MgCl_2$, 25 $NaHCO_3$, 1.25 NaH_2PO_4, 20 glucose, bubbled with 95% O_2/5% CO_2, pH 7.4. Transverse hippocampal slices (300 μm thick) were cut using a vibratome (series 1000 Plus, Technical Products International Inc., St Louis, USA) and stored at 34 °C for 30 min in artificial cerebrospinal fluid (ACSF) containing (in mM): 119 NaCl, 2.5 KCl, 1 NaH_2PO_4, 26 $NaHCO_3$, 1.3 $MgCl_2$, 2.5 $CaCl_2$, 10 glucose, pH 7.4, and equilibrated with 95% O_2/5% CO_2. After a recovery period of at least 1 h at room temperature (22-24 ºC), each slice was individually transferred to the recording chamber and continuously superfused with oxygenated ACSF at a rate of 2-3 ml/min.

Recordings. Pyramidal cells were visualized in the CA3 with an upright microscope (Zeiss Axioskop) equipped with differential interference contrast optics and fluorescence microscopy. Slices were chosen based on having adequate fluorescence in CA3 and broad targeting of the dorsal hippocampus (30-50% of the slices met these criteria). Microelectrodes (5-8 MΩ) were pulled from borosilicate glass capillaries (Sutter Instruments) with a P-97 pipette puller (Sutter Instruments). Membrane potentials were held at V_{hold} = -80 mV for recording spontaneous excitatory postsynaptic currents (sEPSCs) and mini excitatory postsynaptic currents (mEPSCs); spontaneous inhibitory postsynaptic currents (sIPSCs) and mini inhibitory postsynaptic currents (mIPSCs) were recorded at V_{hold} = 0 mV. mEPSCs and mIPSCs were acquired in the presence of tetrodotoxin (TTX, 1 μM) and represent the spontaneous release of individual synaptic vesicles in the absence of action potentials, thereby offering some indication of the relative numbers of synaptic contacts (Schwarz, 2013). sEPCS and sIPSCs represent action potential-evoked transmitter release and provide an indication of ongoing activity. sEPSCs, mEPSCs, sIPSCs, and mIPSCs were each recorded during 5 min of continuous sweeps. The internal solution consisted of (in mM): 130 Cs-CH_3O_3S, 3 CsCl, 1 EGTA, 10 HEPES, 2 NaATP, 0.3 NaGTP, and 10 TRIS phosphocreatine, pH 7.3 adjusted with CsOH, 280-290 mOsm. A criterion for including cells in the analysis was a leak current < 100 pA at $V_{\text{hold}} = -80$ mV. mEPSC/mIPSC and sEPSC/sIPSC values were obtained by calculating the ratios for individual neurons and then averaging the numbers. SLEs were defined as described (Schevon et al., 2012). For perforated patch recordings, the gramicidin stock (1 mg/ml in DMSO) was diluted in the pipette solution (in mM: CsCl 135, $MgCl_2$ 4, HEPES 10, EGTA 0.1, pH 7.4 with CsOH, 280-290 mOsm) to a final concentration of 75-100 μg/ml just before the experiments. The tip of the electrode was filled with gramicidin-free pipette solution. Pipette resistances were 3-5 MΩ. Small voltage steps (-5 mV, 50 ms) were evoked to monitor membrane and access resistances; if one of both or if the holding current changed significantly during the recording, the experiment was discarded. GABA (100 μM, 10 ms, 5 psi) was locally applied every 10 s through a micropipette connected to a Picospritzer coupled with a pulse generator (Master-8, A.M.P.I.). Recordings were performed under voltage-clamp at multiple holding potentials. Peak current amplitudes and their respective holding potentials were plotted to yield the chloride equilibrium potential (E_{Cl}) from a linear fit of the I–V curve for each cell ($R^2 > 0.95$). As a control for perforated-patch integrity, in some cells E_{Cl} was re-determined after breaking into whole-cell configuration: $E_{\text{Cl}} = 2.97 \pm 3.65$ mV (n = 6). All data were collected using a MultiClamp 700A amplifier (Molecular Devices, Sunnyvale, CA, USA), filtered at 2 kHz and digitized at 5 kHz with pCLAMP 9 software (Molecular Devices). Analysis was performed with the Clampfit 9.2 software and MiniAnalysis software. For sEPSC experiments, n = 9 and 6 cells for a-Ctrl and a-101.F, respectively, at P40; at P11, n = 28, 38, and 21 cells for a-Ctrl, a-101.F, and NKCC1-TSB, respectively. For P11 mEPSC and mIPSC experiments, n = 15, 13, 13, and 15 cells for a-Ctrl, a-101.F, NKCC1-TSB, and G1 respectively. For E_{GABA} experiments, n = 8, 7, and 9 cells for a-Ctrl, a-101.F, and NKCC1-TSB, respectively.

E_{GABA} at DIV 8-9. Primary rat hippocampal neurons were plated at a density of 60,000 cells/well on 10 mm coverslips. Cells were transfected at DIV 3 with an antagonist for miR-101b (a-101, 100 nM, Exiqon) or a control sequence (a-Ctrl, 100 nM, Exiqon). Perforated patch-clamp recordings were performed at DIV 8-9. All recordings were carried out at room temperature, using a bath solution containing (in mM): 150 NaCl, 3 KCl, 3 $CaCl_2$, 2 $MgCl_2$, 10 HEPES, and 5 glucose; pH 7.4. Recordings were obtained in the presence of 15 μM CNQX, 25 μM APV, and 1 μM TTX. Gramicidin was diluted from a 1 mg/ml stock in the internal solution (154 mM K-gluconate, 9 mM NaCl, 1mM $MgCl_2$, 10 mM HEPES, and 0.2 mM EGTA; pH 7.4; osmolarity 300 mOsm) to a final concentration of 50

μg/ml immediately before use. Pipettes were pulled from borosilicate glass capillaries (Sutter Instrument) with a P-97 pipette puller and had resistances of 3-4 MΩ. Small voltage steps (10 mV, 50 ms) were evoked before each application of GABA to monitor membrane and access resistances. If the holding current or resistance significantly changed during the recording, the experiment was discarded. Recordings were carried out using a MultiClamp 700A patch clamp amplifier. Signals were filtered at 2 kHz, sampled at 5 kHz, and analyzed using Clampfit 9.2 software. GABA (100 μM, 10 ms, 5 psi) was locally applied every 10 s through a micropipette connected to a Picospritzer. Recordings were performed under voltage clamp at multiple holding potentials. Peak current amplitudes and their respective holding potentials were plotted to yield the chloride equilibrium potential (E_{Cl}) from a linear fit of the I–V curve for each cell. As a control for perforated-patch integrity, in some cells E_{Cl} was re-determined after establishing a whole-cell configuration and adjusting the intracellular chloride concentration to yield a dramatic hyperpolarization of E_{Cl} (-85.73 ± 1.07 mV, n=3). For E_{GABA} experiments in culture, n = 8 and 7 cells for a-Ctrl and a-101.F, respectively.

Behavior

Animals. Male and female mice were injected at P2 as described (a-Ctrl, n = 24; a-101.F, n = 29), weaned at 4 weeks of age, and housed 6 per cage under 12/12 h light/dark cycle (07:00 AM-07:00 PM) at 23 ± 1°C, with free access to food and water. All animals survived the treatment and showed no gross behavioral alterations. Behavioral testing began when mice were 8 week-old and was always performed from 10:00 AM to 04:00 PM. Before each test mice were allowed to habituate to the testing room for 30 min.

Fear conditioning. Fear conditioning procedures were based on published methods (Corradi et al., 2008; Zanardi et al., 2007). Briefly, mice were transferred to a noise insulated conditioning chamber (23 x 22 x 24 cm) with grey Plexiglas walls and ceiling, and, after an initial acclimatization period of 2 min, were presented with 3 pairings of the tone with foot shock (0.5 mA, 2 s). The tone was presented for 30 s and the shock was administered during the last 2 s of the tone. Pairings were separated by 2 min and mice were removed from the chamber 30 s after the last shock presentation.

Approximately 24 h after conditioning, mice were tested for contextual conditioning. Mice were placed into the conditioning chamber for 5 min and freezing behavior was scored. Mice were then transferred to an altered context (20 x 20 x 20 cm clear plastic cage that was covered with a filter lid) and tested for freezing for 3 min (altered context test) and then for 3 min during presentation of the tone (cued conditioning test).

Freezing was scored using a time sampling procedure in which a determination was made at 10 s intervals. Freezing was defined as the absence of all movements except for respiration for a minimum of 1 s.

Alternation test. Spontaneous alternations were assessed using a symmetrical Y-maze as described in Zanardi et al., 2007 with slight modifications. This test is used to study hippocampal function in young rodents (reviewed by Albani et al., 2014). Spontaneous alternation in rodents requires a functionally intact dorsal hippocampus (Dillon et al., 2008), and maze navigation is guided by visual contextual cues (Douglas et al., 1966). The maze was constructed of black plastic and placed inside a box with 4 extra-maze visual cues, one on each wall. Each arm was 22 cm long x 10 cm high x 7 cm wide, and the three arms were connected through a symmetrical 3-way central corridor. Arms were randomly designated as A, B, or C. Mice were allowed to roam freely through the maze during an 8 min trial, and the series of arm entries was recorded. Alternation was defined as entries into all three arms consecutively (i.e., ABC, ACB, CAB, etc.) and an entry was considered valid only when the animal had 4 paws inside the arm. The maximum number of alternations was, therefore, the total number of arm entries minus two, and the percentage of alternation was calculated as [actual number of alternations/maximum number of alternations] x 100. The arena was thoroughly wiped with 70% ethanol after each test to avoid olfactory cues.

Object/Place Recognition Test. Object/place recognition was assessed as previously described (Binder et al., 2012; Vogel-Ciernia et al., 2013) with slight modifications. Briefly, the animals were tested in a wooden box (45 x 30 cm) with neutral grey floor and black walls. Black and white spatial cues were taped on each wall. Habituation consisted of a 5 min period in the empty cage the day before the test. On the testing day, the mice were exposed for 5 min to a pair of identical objects, placed on the central line of the cage at a distance of 20 cm from each other. The objects were previously shown to induce enough time of exploration in the mice. Three h after the initial exposure, mice were re-exposed for 5 min to the same cage, with one object of the original pair in the same position as it was in the first trial (referred to as the “old-place object”), and the second one randomly moved in one of the corners of the cage (referred to as the “new-place object). In all tests, time spent exploring each object was recorded. A mouse was considered to be engaging in exploratory behavior if the animal touched the object with its forepaw or nose or sniffed at the object within a distance of 1.5 cm.

Open Field. Exploratory behavior and anxiety were assessed with the open-field test. The test was conducted in an open wooden chamber (50 x 50 x 30 cm) with white walls and white floor. The arena was virtually divided in a peripheral zone (within 10 cm of the walls) and a central zone (the rest of the arena). Mice were placed in the center of the arena and allowed to explore for 10 min. Travelled distance and time spent in each zone were recorded and automatically analyzed with ANY-Maze (Stoelting) video tracking software. The arena was thoroughly wiped with 70% ethanol after each test to avoid olfactory cues.

Elevated plus maze. Animals were tested in an opaque gray Plexiglas plus maze, with 30 cm long, 7 cm wide arms joined at the center by a 7 cm platform, elevated 40 cm above the ground. The 2 "closed" arms have sidewalls 17 cm high but open on the top. The room was brightly lit (100 lux). At the beginning of the test, a mouse was placed in the center of the maze in a cylinder (diameter: 7 cm, 15 cm high) for 30 s before being allowed to explore the maze for 8 min. An entry was counted only when the mouse entered an arm with all four feet. Three measures were taken: 1) the time spent in the open arms divided by the total time spent in all arms of the maze (time ratio); 2) the number of entries into the open arms divided by the total number of entries into all arms (entry ratio); 3) the total distance travelled.

Slice preparation and confocal imaging of spontaneous calcium transients

Calcium imaging at P8 in CA3. We adapted the protocol from Crepel et al., 2007. Briefly C57BL6J (Harlan) P8 male mice were anesthetized with Ketamine/Xylazine and sacrificed by decapitation. Acute coronal slices (300 μm) were prepared using a Leica vibratome with ice-cold oxygenated slicing solution as described above. We obtained 3-4 coronal slices containing both dorsal hippocampi per animal. Slices were examined with an epifluorescent microscope to confirm broad a-101.F fluorescence (on average 50-75% of slices). To load the calcium indicator, slices were transferred into a sealed 1.5 ml tube containing 5 μM Fluo-4AM (Molecular Probes, 50% DMSO, 50% Pluronic Acid) diluted in oxygenated modified artificial cerebrospinal fluid (mACSF) at 35°C, for 30 min, in the dark. The mACSF (also used as imaging solution) contained (in mM): 126 NaCl, 3.5 KCl, 1.2 NaH_2PO_4, 26 $NaHCO_3$, 1.0 $MgCl_2$, 2.0 $CaCl_2$, and 10 glucose, pH 7.4. Slices were then dissected along the midline and transferred to a slice holder where they were maintained at room temperature in the dark for an additional h before imaging. Experiments were performed in a custom-made chamber that allowed constant perfusion with aerated mACSF at 1-2 ml/min. A Leica SP5 multiphoton microscope (Leica Microsystems, Germany) with a low-magnification (10X) water immersion objective was used for imaging. Bi-directional scanning was used at a 400 Hz imaging rate, with a time resolution of 328 ms. The image field was typically 620 x 310 μm. For calcium imaging at P8, n = 22, 13, 18, 20, and 25 movies from animals receiving a-Ctrl, a-101.F, G1, G2, or G3, respectively. Each condition included 8-12 animals from 3-5 litters.

Calcium imaging at P40 in the DG. We adapted the "protective recovery" protocol from Peca et al., 2011 and Chen et al., 2012. Briefly, mice are anesthetized with Ketamine/Xylazine and perfused through the heart with 10 ml of ice-cold oxygenated slicing solution containing (in mM): 93 N-methyl-D-glucamine (NMDG), 20 Hepes, 2.5 KCl, 1.2 NaH_2PO_4, 30 $NaHCO_3$, 25 glucose, 10 $MgSO_4$, 0.5 $CaCl_2$, 5 sodium ascorbate, 3 sodium pyruvate, 2 thiourea, pH 7.4. Acute coronal slices (400 μm) were prepared using ice-cold oxygenated cutting solution. On average we obtained 4-5 coronal slices containing both dorsal hippocampi per animal. Slices were allowed to recover for 15 min at 35°C and then were transferred to oxygenated mACSF at room temperature for another h. Slices were then dissected along the midline and transferred to a slice holder where they were maintained at room temperature in the dark for an additional h before imaging. The distribution of GCaMP6f fluorescent signal was used as an indicator of the P2 LNA/virus injection. A strong fluorescent signal in CA1 and DG indicated widespread infection (40-60% of all slices). In fact, very likely the viral infection also included the CA3 but would not be apparent because the synapsin1 promoter driving GCaMP6f is readily expressed in CA1 pyramidal neurons and DG cells (Figure S3D) but not in CA3 pyramidal neurons. *In vivo* ready LNAs are able to quickly spread further because of their small size, and they target all cell types because of their chemistry, i.e. LNAs are not cell-type selective (Figure S2A). Calcium imaging was performed as described above. TTX (1 μm) treatment of P40 acute hippocampal slices during calcium imaging was used to demonstrate that all of the activity measured depends on action potentials. For calcium imaging at P40, n = 21, 17, 20, and 18 movies for a-Ctrl, a-101.F, NKCC1-TSB, and G1, respectively, employing 4-12 animals from 2-3 litters each. For calcium imaging at P40 in animals injected at P30 (acute LNA injection), n = 13 and 20 movies for a-Ctrl and a-101.F respectively, employing 5-6 animals for each group.

Calcium imaging analysis. To remove artifacts due to minor movements during recording, movies were aligned using the ImageJ (RRID:SCR_003070) Stack – Shuffling plugin and exported as a .tiff file. A custom-made analysis pipeline was developed using Matlab (Math-Works; RRID:SCR_001622) and the imaging computational microscope (Frady et al., 2015 and 20156). In this pipeline, cells in the field of view were automatically detected using principal and independent components analysis (Mukamel et al., 2009) (PCA; ICA). Both PCA and ICA are linear component decompositions, and when applied to imaging data produce several components, each of which has a “source” and a “map”. Sources are the time series of the extracted components, and maps show their spatial distributions. The PCA algorithm analyzes the variance of the pixels in the imaging data and finds the projections that account for the most variance, with constraints on orthogonality. PCA is used as a preprocessing step for ICA, which seeks independence in the projections. The ICA algorithm extracts both artifacts and neuronal signals as components; the artifacts can be quickly sorted by looking through the sources and maps with ICM. Regions of interest (ROIs) were generated automatically by the algorithm, by segmenting the spatial maps of the independent components, and then were refined manually to target neurons that respond to the KCl-induced depolarization at the end of each imaging trial. Only cells that showed KCl depolarization were chosen for further analysis. Cells that had very slow calcium responses (>5 sec) were excluded, on the basis that they were most likely glia. The calcium signal trace for each cell was obtained by averaging the fluorescence within that ROI as a function of time.

Several movies showed a photo-bleaching-induced decrease in baseline fluorescence that we adjusted as following. Visual inspection showed that filtering by standard detrending of the fluorescence data (fitting a polynomial to the data) could not provide a stationary result: the spikes would dominate the fitting. Thus, we first smoothed the data by applying a band-pass filter (cutting high-frequency oscillations); then we determined a "support line" (SL), precisely a cubic curve underneath the smoothed series whose distance from the series was minimum. The filtered series was the difference between the series and SL. The KCl-induced depolarization at the end of the movie was not included to compute SL. A manual threshold (normally ≥ 3-fold the standard deviation of baseline fluorescence or F_0) was used to identify calcium events. The synchronized events (SEs) were detected by selecting the principal component (PC) that corresponded manually using ICM, which was typically the first or second PC. Because these events were correlated and accounted for a lot of variance in the data, they were easily extracted by PCA. The number of SEs was determined by comparing raster plots of all calcium events extracted with ROIs with the corresponding PC that signifies the event (Figure 4A and 4B). The number of cells participating in each SE was determined by counting how many cells, out of all viable cells, had calcium events in the time window of 984 ms before and after the peak of the SE. Asynchronous events were all events that were not included in the time window of each SE. Data from each movie were then transferred to Excel (Microsoft) for consolidation, and statistical analysis was performed in Prism (GraphPad).

Calcium imaging in primary neurons

The protocol used was modified from Ganguly et al., 2001, and Liu et al., 2006. Primary rat hippocampal neurons were obtained as described (Lozada et al., 2012) and plated on glass-bottom 35 mm culture dishes. At DIV3, neurons were transfected using 4 μl/ml of siPORT NeoFX transfection reagent (Invitrogen) and a-101 (a non-fluorescent version of a-101.F) at a concentration of 100 nM. Calcium imaging was performed at DIV8 and DIV10. To load the calcium indicator, the culture medium was replaced with oxygenated Hank's Balanced Salt Solution (HBSS) containing 5 μM Fluo-4, AM (Molecular Probes, 50% DMSO, 50% pluronic Acid), 20 μM NBQX (Tocris) and 10 μM bicuculline methiodide (BMI, Tocris) and left at room temperature, in the dark for 30 min. HBSS contained (in mM): 150 NaCl, 3 KCl, 3 $CaCl_2$, 2 $MgCl_2$, 10 Hepes, 5 glucose. Recordings were performed in the presence of 20 μM NBQX to record exclusively GABAergic activity. A Zeiss Axiovert S100 inverted fluorescence microscope equipped with a QIClick digital CCD camera (QImaging) was used for imaging. SlideBook 6 (3i) imaging software was used for acquisition at 2 frames/s and recording. The baseline fluorescence was recorded for 30 s and then 400 μM GABA was added to the culture dish. Because NBQX suppresses glutamatergic activity, baseline fluorescence in viable neurons was very low and stable. Lastly 1 M KCl was added 45 s after the GABA application to identify all viable neurons in the field of view. Movies were analyzed with ImageJ, and ROIs were drawn manually using the KCl response as reference. The threshold was set at 150% $\Delta F/F_0$ (the variation in fluorescence divided by the baseline fluorescence) to identify both the GABA and KCl response. A $\Delta F/F_0$ threshold takes into account variations in baseline fluorescence and only identifies true GABA responders. Cells that did not respond to KCl were excluded. Calcium imaging values were pooled from 4-5 separate experiments with 3-5 movies per experiment.

Luciferase assay

The luciferase assay was performed using a custom-made pEZX-MT01 miTarget miRNA target Sequence 3' UTR Expression clone (GeneCopoeia) in which the full NKCC1 3'-UTR was cloned downstream of the luciferase gene (hLuc). The construct also contained a Renilla reporter (hRLuc) to normalize for transfection efficiency.

HEK293T cells were plated on a 96-well micro-plate and transfected when 30% confluent with a-101/a-Ctrl and siPORT transfection reagent as above. The next day cells were transfected with the pEZX plasmid (300 ng/well) using calcium phosphate (Halff et al., 2014). Fetal bovine serum in the medium was reduced to 1% to slow cell growth. The luciferase assay was performed 3 days later using the Luc-Pair miR Luciferase Assay (GeneCoepia) and following manufacturer's instructions. A micro-plate reader with built-in reagent injectors (Berthold Technologies) was used for automated delivery of Luciferase and Renilla substrates. Luminescence was recorded with Magellan 5 software. Results were pooled from 3 separate experiments with 24 wells per experiment for each condition.

Sensor Experiments

MiR-101 sensor. The miR-101b lentiviral sensor was created from the lentiviral miR-19 tracer (Han et al., 2016; a generous gift from Dr. Fred Gage). GFP is expressed constitutively from a miniCMV promoter, while CAG drives expression of RFP followed by miR-19 MREs. The RFP and miR-19 sites were removed with BamHI and KpnI, and were replaced with an insert containing RFP_{670} (Addgene) and 6 perfectly complementary miR-101b sequences in the 3' UTR. A control sensor (not sensitive to any miRs) was cloned by inserting RFP_{670} with no known miRNA sequences in the 3' UTR. Lentivirus was packaged as described (Han et al., 2009; Boyden et al., 2005).

Purified and concentrated lentiviral sensor was combined with a-101.F (to give 0.5 µM a-101.F), and injected into P2 animals. For these experiments a version of a-101.F labeled with TYE-563 was used to avoid interfering with the GFP. At P7, animals were perfused with PBS followed by 4% paraformaldehyde, and brains were removed and postfixed overnight in 4% PFA. Brains were cryoprotected in 30% sucrose in PBS until they sank. Sections (40 µm) were obtained on a sliding microtome (Leica), mounted onto slides, and coverslipped with VectaShield. No enhancement of fluorescence was performed. Slides were imaged on a Leica SP5 laser scanning confocal microscope. Virally-infected cells were identified by GFP fluorescence, and Z-stacks (at 2 µm steps) were taken through the entire section using a 20X oil immersion objective. Acquisition settings (laser power, gain, offset) for GFP and RFP_{670} remained identical for all conditions. Max projections of z-stacks were analyzed in ImageJ. ROIs were drawn using the GFP channel, and the average fluorescence intensity was measured in both the GFP and RFP_{670} channels. The ratio of RFP_{670} to GFP fluorescence was compared between the control sensor and the miR-101b sensor in the presence of either a-Ctrl or a-101.F LNAs. Six-ten images were analyzed from 3-4 animals in each condition.

MiR-101 targets sensors. The miR-101 sensor construct was adapted to validate Ank2, Kif1a, and NKCC1 as *bona fide* miR-101 targets, as previously described (Thiebes et al., 2015). The 6 perfectly complementary miR-101 sequences were replaced with the endogenous miR-101 MREs (wild-type) or a mutated version of the MREs in which 4 of the seed bases were substituted. The mutated sequence was blasted against all known miRs (miRBase) to make sure that it did not recognize any other miRs. Viral preparation, injections, and analysis were performed as described above.

Fluorescent in situ hybridization of miRs

Six week-old C57Bl6J mice were anesthetized with chloral hydrate (400 mg/kg, i.p.). All procedures were conducted in RNAse-free conditions using Diethylpyrocarbonate (DEPC) pre-treated solutions. Intracardial perfusion was performed with 50 mL of 0.9% NaCl containing heparin sodium (5000U/L) followed by 4% paraformaldehyde (PFA) in DEPC-PBS (70 mL/7 min). The brains were post-fixed in the same solution for 12 h and rinsed in 20% sucrose in PBS-DEPC for 1 day. The brains were frozen using dry ice, and coronal 50 µm thick sections were cut at a cryostat, washed three times in cold 1x PBS-DEPC, and immediately processed for microRNA detection.

Fluorescent in situ hybridization (FISH) was performed using miRCURY LNA™ microRNA ISH Optimization Kit and 5′ and 3′ digoxygenin labeled LNA (DIG-labeled-LNA) probes (Exiqon) as described by the manufacturer's instructions with minor modifications. Briefly, freshly cut brain sections were post-fixed with 4% PFA for 10 min at room temperature (RT) followed by treatment with 3% H_2O_2. Then, sections were incubated in freshly diluted proteinase K (PK) (5µg/mL) at 37°C for 10 min. After 3 washes in DEPC-PBS at RT, sections were incubated with DIG-labeled-LNA miR probe for 1h at the following hybridization temperature (HybT) in microRNA ISH buffer: 60°C for U6 snRNA and miR-124 probes, 55°C for miR-101a and Scramble-miR probes. After stringent washes at HybT and blocking, sections were incubated with an anti-DIG- antibody (1:100; Roche) 1h at RT and developed using Cy3-tyramide kit (PerkinElmer) for 10 min at RT. Sections were stained with NeuroTrace® 530/615 Red Fluorescent Nissl Stain (Applied Biosystem) according to manufacturer's instructions, counterstained with DAPI and cover- slipped for confocal microscopy analysis. Sections hybridized with U6 snRNA showed accumulation of strong fluorescent spots over cell bodies identified by DAPI staining throughout the section, whereas sections hybridized with Scramble-miR showed a low level of homogeneously dispersed fluorescent spots throughout the tissue.

Immunocytochemistry

Male mice were anesthetized with ketamine/xylazine and then transcardially perfused at a fixed rate, using a peristaltic pump, with ice-cold PBS followed by 4% PFA. Brains were post-fixed overnight and then cryoprotected in PBS containing 25% sucrose for at least 2 days. Brains were then sectioned coronally at 40 μm with a microtome (Leica, SM210R).

Immunostaining was performed free-floating in 24-well plates. Fixed 40-μm-thick brain sections were permeabilized at room temperature for 1 h in PBS, pH 7.4, with 0.3% Triton X-100 (PBST) and 5% donkey serum (DS). Slices were then transferred to a solution containing 0.3% PBST, 5% DS, and the primary antibody (VGlut1, 1:500, AB5905 Millipore, RRID:AB_2301751; GFAP, 1:1000, G3893 Sigma, RRID:AB_477010; Ki1a, 1:200, sc-19106 Santa Cruz Biotechnology, RRID:AB_2131408; Ank2, 1:100, AB192769 Abcam) and incubated overnight at 4°C. Sections were then washed three times with PBS and incubated with secondary antibodies (donkey anti-guinea pig CF488A, 1:500, 20169-1 Biotium, AB_10853117; donkey anti-mouse Alexa 488, 1:500, A21202 Invitrogen, RRID:AB_2535788; donkey anti-goat Alexa 555, 1:500, A21432 Invitrogen, RRID:AB_141788; donkey anti-mouse Alexa 555, 1:500, A31570 Invitrogen, RRID:AB_2536180). Sections were washed three more times in PBS, stained with the far-red DNA stain Draq5 (62254 ThermoFisher), and mounted with medium (Vectashield; Vector Laboratories). Nonspecific immunostaining was assessed by substituting nonimmune IgG for the primary antibody and found to be negligible.

Fluorescence images were obtained with a Leica TCS SP5 confocal microscope using ImageJ for particle analysis. Confocal scans were performed in the CA3 region of the dorsal hippocampus at P8, P15, or P30. Imaging and analysis parameters were identical for all groups. For the VGlut1 particle analysis, images were taken in the stratum radiatum (60 μm from the pyramidal cell layer, beyond the mossy fibers in the stratum lucidum) where commissural associations are prevalent. To minimize antibody penetration problems, three merged optical sections localized close to the tissue surface were used per slice (2 images per slice, 2 slices per animal). The three merged optical sections were analyzed using the ImageJ particle analysis, nucleus counter plugin (Size =10-300, watershed filter = ON). Data were collected from two 16x16 μm images per slice, two slices per animal from 4-5 male P15 mice for each group (from 7 litters).

Analysis of dendritic complexity and dendritic spines

For the analysis of dendritic structure at P8 and dendritic protrusions at P11, we took advantage of a glycoprotein-deleted variant of the SAD-B19 strain of rabies virus encoding eGFP (SAD Δ G-eGFP) that functions as a retrograde tracer of synaptically connected neurons (Ginger et al., 2013). SAD Δ G-eGFP injected directly into the hippocampus sparsely labels CA1 pyramidal neurons (through recurrent connections or local interneurons) and CA3 pyramidal neurons (through A/C, Schaffer collaterals, and local interneurons). Male animals were injected at P2 and brain perfusion-fixed at P8 for analysis of dendritic complexity and at P11 for analysis of dendritic protrusions (injection and perfusion techniques described above). Brains were then sectioned coronally at 80 μm with a microtome to preserve the entire dendritic structure.

Confocal z-stacks of intact neurons were acquired with a Leica TCS SP5 microscope using a 20X lens. Analysis was performed with the help of the NeuronJ (Meijering et al., 2004) plugin for ImageJ, distinguishing primary and secondary structures of the apical dendrite from CA1 and CA3 pyramidal neurons. Data were collected from 3-6 littermates per group (3 litters), 14-30 primary dendrites and 48-100 secondary dendrites per group.

High-resolution images of dendritic protrusions were acquired with a Leica TCS SP5 microscope using a 63X lens. Classification of protrusions as filopodia, thin spines, mushroom spines, and stubby spines was done as previously described (Lippi et al., 2011). Data were collected from 3-6 littermates per group (3 litters), 11-36 primary dendrites per group.

Western Blot Analysis

NKCC1 protein levels. Brain slices from a-Ctrl injected controls and a-101.F injected mice (12 and 14 animals respectively, 4-5 slices per animal) were collected using a vibratome (series 1000 Plus, Technical Products International Inc., St Louis, USA). Subcellular protein fractionation was performed using the ProteoExtract Subcellular Proteome Extraction Kit (Calbiochem). Protein amounts in the obtained fractions were determined by Non-Interfering Protein Assay Kit (Calbiochem). Protein samples were separated by sodium dodecyl sulfate-polyacrylamide gel electrophoresis and blotted to nitrocellulose membranes (Biorad). The membranes were blocked with 5% non-fat dry milk in PBS containing 0.1% Tween 20 and incubated overnight with the primary antibodies: NKCC1 (1:1000; Developmental Studies Hybridoma Bank, University of Iowa), Beta-Actin (1:12000, Sigma-Aldrich). Protein bands were then detected using the enhanced chemiluminescent substrate kit (EMD Millipore).

Statistics

All data sets were tested for normal distribution and equal variances. Departure from normality was assessed with 2 sample Kolmogorov-Smirnov test or D'Agostino-Pearson omnibus normality test. The variance was calculated with F-test. Grubbs' test was used to exclude outliers from normally distributed data sets.

Two-groups comparison. Unpaired Student's t-test was used for all experiments with normal distribution and equal variances. Welch's t-test was used when the variances were not equal. Mann-Whitney U test was used for datasets that were not normally distributed. The 2 sample Kolmogorov-Smirnov test was used to compare distributions.

Three- or more groups comparison. One-way analysis of variance (ANOVA), followed by a Tukey's multiple comparison test, was used for experiments with normal distribution. Kruskal-Wallis' test followed by a Dunn's multiple comparisons test was used for datasets that were not normally distributed.

For all tests, $p<0.05$ was used as threshold for significant difference. For all tests P values are two-tailed.

Sample size. Sample size for animal studies was based on established criteria extrapolated from the existing literature. A power analysis tool (Statistical Solutions) helped us to determine group sizes for all experiments. For example, to determine how many movies we needed to see a difference in SEs, we assumed $\mu = 2$ SEs/min, $\sigma = 50\%$ of the control group mean, and $\mu_1 = 150\% \ \mu$. With these assumptions, a sample size of 12 is required to achieve a power of 0.8. Randomization was used to allocate animals across the treatment groups. It was also used to determine which animals or slices were tested first during behavior, electrophysiological, and calcium imaging recordings.

SUPPLEMENTAL REFERENCES

Adesnik, H., Li, G., During, M.J., Pleasure, S.J., and Nicoll, R.A. (2008). NMDA receptors inhibit synapse unsilencing during brain development. Proc Natl Acad Sci U S A *105*, 5597-5602.

Albani, S.H., McHail, D.G., and Dumas, T.C. (2014). Developmental studies of the hippocampus and hippocampal-dependent behaviors: insights from interdisciplinary studies and tips for new investigators. Neurosci Biobehav Rev *43*, 183-190.

Bannai, S. (1986). Exchange of cystine and glutamate across plasma membrane of human fibroblasts. J Biol Chem *261*, 2256-2263.

Barres, B.A., and Smith, S.J. (2001). Neurobiology. Cholesterol--making or breaking the synapse. Science *294*, 1296-1297.

Benham, C.D., Evans, M.L., and McBain, C.J. (1992). Ca2+ efflux mechanisms following depolarization evoked calcium transients in cultured rat sensory neurones. J Physiol *455*, 567-583.

Binder, S., Baier, P.C., Molle, M., Inostroza, M., Born, J., and Marshall, L. (2012). Sleep enhances memory consolidation in the hippocampus-dependent object-place recognition task in rats. Neurobiol Learn Mem *97*, 213-219.

Boyden, E.S., Zhang, F., Bamberg, E., Nagel, G., and Deisseroth, K. (2005). Millisecond-timescale, genetically targeted optical control of neural activity. Nat Neurosci *8*, 1263–1268.

Brini, M., Cali, T., Ottolini, D., and Carafoli, E. (2013). The plasma membrane calcium pump in health and disease. FEBS J *280*, 5385-5397.

Cattani, A.A., Bonfardin, V.D., Represa, A., Ben-Ari, Y., and Aniksztejn, L. (2007). Generation of slow network oscillations in the developing rat hippocampus after blockade of glutamate uptake. J Neurophysiol *98*, 2324-2336.

Cavazos, J.E., Golarai, G., and Sutula, T.P. (1991). Mossy fiber synaptic reorganization induced by kindling: time course of development, progression, and permanence. J Neurosci *11*, 2795-2803.

Chen, Q., Cichon, J., Wang, W., Qiu, L., Lee, S.J., Campbell, N.R., Destefino, N., Goard, M.J., Fu, Z., Yasuda, R., *et al.* (2012). Imaging neural activity using Thy1-GCaMP transgenic mice. Neuron *76*, 297-308.

Corradi, A., Zanardi, A., Giacomini, C., Onofri, F., Valtorta, F., Zoli, M., and Benfenati, F. (2008). Synapsin-I- and synapsin-II-null mice display an increased age-dependent cognitive impairment. J Cell Sci *121*, 3042-3051.

Crepel, V., Aronov, D., Jorquera, I., Represa, A., Ben-Ari, Y., and Cossart, R. (2007). A parturition-associated nonsynaptic coherent activity pattern in the developing hippocampus. Neuron *54*, 105-120.

De Bundel, D., Schallier, A., Loyens, E., Fernando, R., Miyashita, H., Van Liefferinge, J., Vermoesen, K., Bannai, S., Sato, H., Michotte, Y., *et al.* (2011). Loss of system x(c)- does not induce oxidative stress but decreases extracellular glutamate in hippocampus and influences spatial working memory and limbic seizure susceptibility. J Neurosci *31*, 5792-5803.

Demarque, M., Represa, A., Becq, H., Khalilov, I., Ben-Ari, Y., and Aniksztejn, L. (2002). Paracrine intercellular communication by a Ca2+- and SNARE-independent release of GABA and glutamate prior to synapse formation. Neuron *36*, 1051-1061.

Dillon, G.M., Qu, X., Marcus, J.N., and Dodart, J.C. (2008). Excitotoxic lesions restricted to the dorsal CA1 field of the hippocampus impair spatial memory and extinction learning in C57BL/6 mice. Neurobiol Learn Mem *90*, 426-433.

Douglas, R.J. (1966). Cues for spontaneous alternation. J Comp Physiol Psychol *62*, 171-183.

Durand, G.M., Kovalchuk, Y., and Konnerth, A. (1996). Long-term potentiation and functional synapse induction in developing hippocampus. Nature *381*, 71-75.

Eacker, S.M., Keuss, M.J., Berezikov, E., Dawson, V.L., and Dawson, T.M. (2011). Neuronal activity regulates hippocampal miRNA expression. PLoS One *6*, e25068.

Empson, R.M., Garside, M.L., and Knopfel, T. (2007). Plasma membrane Ca2+ ATPase 2 contributes to short-term synapse plasticity at the parallel fiber to Purkinje neuron synapse. J Neurosci *27*, 3753-3758.

Ewell, L.A., Liang, L., Armstrong, C., Soltesz, I., Leutgeb, S., and Leutgeb, J.K. (2015). Brain state is a major factor in preseizure hippocampal network activity and influences success of seizure intervention. J Neurosci *35*:15635–48.

Ferraro, T.N., Golden, G.T., Smith, G.G., St Jean, P., Schork, N.J., Mulholland, N., Ballas, C., Schill, J., Buono, R.J., and Berrettini, W.H. (1999). Mapping loci for pentylenetetrazol-induced seizure susceptibility in mice. J Neurosci *19*, 6733-6739.

Flugge, G., Araya-Callis, C., Garea-Rodriguez, E., Stadelmann-Nessler, C., and Fuchs, E. (2014). NDRG2 as a marker protein for brain astrocytes. Cell Tissue Res *357*, 31-41.

Frady, E.P., Kapoor, A., Horvitz, E., Kristan, W.B. (2016). Scalable semi-supervised functional neurocartography reveals canonical neurons in behavioral networks. Neural Comput *28*, 1453-97.

Frady, E.P., Kristan, W.B. (2015). The Imaging Computational Microscope. arXiv:1502.07009.

Ganguly, K., Schinder, A.F., Wong, S.T., and Poo, M. (2001). GABA itself promotes the developmental switch of neuronal GABAergic responses from excitation to inhibition. Cell *105*, 521-532.

Ganor, Y., Goldberg-Stern, H., Cohen, R., Teichberg, V., and Levite, M. (2014). Glutamate receptor antibodies directed against AMPA receptors subunit 3 peptide B (GluR3B) can be produced in DBA/2J mice, lower seizure threshold and induce abnormal behavior. Psychoneuroendocrinology *42*, 106-117.

Ginger, M., Haberl, M., Conzelmann, K.K., Schwarz, M.K., and Frick, A. (2013). Revealing the secrets of neuronal circuits with recombinant rabies virus technology. Front Neural Circuits *7*, 2.

Gomez-Varela, D., Schmidt, M., Schoellerman, J., Peters, E.C., and Berg, D.K. (2012). PMCA2 via PSD-95 controls calcium signaling by alpha7-containing nicotinic acetylcholine receptors on aspiny interneurons. J Neurosci *32*, 6894-6905.

Halff, A.W., Gomez-Varela, D., John, D., and Berg, D.K. (2014). A novel mechanism for nicotinic potentiation of glutamatergic synapses. J Neurosci *34*, 2051-2064.

Han, J., Kim, H.J., Schafer, S.T., Paquola, A., Clemenson, G.D., Toda, T., Oh, J., Pankonin, A.R., Lee, B.S., Johnston, S.T., Sarkar, A., Denli, A.M., and Gage, F.H. (2016). Functional Implications of miR-19 in the Migration of Newborn Neurons in the Adult Brain. Neuron *91*, 79-89.

Han, X., Qian, X., Bernstein, J.G., Zhou, H.H., Franzesi, G.T., Stern, P., Bronson, R.T., Graybiel, A.M., Desimone, R., and Boyden, E.S. (2009). Millisecondtimescale optical control of neural dynamics in the nonhuman primate brain. Neuron *62*, 191–198.

He, M., Liu, Y., Wang, X., Zhang, M.Q., Hannon, G.J., and Huang, Z.J. (2012). Cell-type-based analysis of microRNA profiles in the mouse brain. Neuron *73*, 35-48.

Hollander, J.A., Im, H.I., Amelio, A.L., Kocerha, J., Bali, P., Lu, Q., Willoughby, D., Wahlestedt, C., Conkright, M.D., and Kenny, P.J. (2010). Striatal microRNA controls cocaine intake through CREB signalling. Nature *466*, 197-202.

Huang da, W., Sherman, B.T., and Lempicki, R.A. (2009). Systematic and integrative analysis of large gene lists using DAVID bioinformatics resources. Nat Protoc *4*, 44-57.

Jasmin, S.B., Pearson, V., Lalonde, D., Domenger, D., Theroux, L., and Poirier, J. (2014). Differential regulation of ABCA1 and ABCG1 gene expressions in the remodeling mouse hippocampus after entorhinal cortex lesion and liver-X receptor agonist treatment. Brain Res *1562*, 39-51.

Jimenez-Mateos, E.M., Engel, T., Merino-Serrais, P., McKiernan, R.C., Tanaka, K., Mouri, G., Sano, T., O'Tuathaigh, C., Waddington, J.L., Prenter, S.*, et al.* (2012). Silencing microRNA-134 produces neuroprotective and prolonged seizure-suppressive effects. Nat Med *18*, 1087-1094.

Jovicic, A., Roshan, R., Moisoi, N., Pradervand, S., Moser, R., Pillai, B., and Luthi-Carter, R. (2013). Comprehensive expression analyses of neural cell-type-specific miRNAs identify new determinants of the specification and maintenance of neuronal phenotypes. J Neurosci *33*, 5127-5137.

Karasinska, J.M., Rinninger, F., Lutjohann, D., Ruddle, P., Franciosi, S., Kruit, J.K., Singaraja, R.R., Hirsch-Reinshagen, V., Fan, J., Brunham, L.R.*, et al.* (2009). Specific loss of brain ABCA1 increases brain cholesterol uptake and influences neuronal structure and function. J Neurosci *29*, 3579-3589.

Klein, M.E., Lioy, D.T., Ma, L., Impey, S., Mandel, G., and Goodman, R.H. (2007). Homeostatic regulation of MeCP2 expression by a CREB-induced microRNA. Nat Neurosci *10*, 1513-1514.

Leutgeb, J.K., Leutgeb, S., Treves, A., Meyer, R., Barnes, C.A., McNaughton, B.L., Moser, M.B., and Moser, E.I. (2005). Progressive transformation of hippocampal neuronal representations in "morphed" environments. Neuron *48*, 345-358.

Liu, L., Shi, M., Wang, L., Hou, S., Wu, Z., Zhao, G., and Deng, Y. (2012). Ndrg2 expression in neurogenic germinal zones of embryonic and postnatal mouse brain. J Mol Histol *43*, 27-35.

Livak, K.J., and Schmittgen, T.D. (2001). Analysis of relative gene expression data using real-time quantitative PCR and the 2(-Delta Delta C(T)) Method. Methods *25*, 402-408.

Lozada, A.F., Wang, X., Gounko, N.V., Massey, K.A., Duan, J., Liu, Z., and Berg, D.K. (2012). Glutamatergic synapse formation is promoted by alpha7-containing nicotinic acetylcholine receptors. J Neurosci *32*, 7651-7661.

Mankin, E.A., Sparks, F.T., Slayyeh, B., Sutherland, R.J., Leutgeb, S., and Leutgeb, J.K. (2012). Neuronal code for extended time in the hippocampus. Proc Natl Acad Sci U S A *109*, 19462-19467.

Mares, P. Kubova, H. (2006) Electrical stimulation-induced models of seizures. In: Models of seizures and epilepsy. Eds: Pitkanen, A., Schwartzkroin, P.A. & Moshe, S.L. Elsevier academic press. 153-159.

Meijering, E., Jacob, M., Sarria, J.C., Steiner, P., Hirling, H., and Unser, M. (2004). Design and validation of a tool for neurite tracing and analysis in fluorescence microscopy images. Cytometry A *58*:167–176.

Mukamel, E.A., Nimmerjahn, A., and Schnitzer, M.J. (2009). Automated analysis of cellular signals from large-scale calcium imaging data. Neuron *63*, 747-760.

Peca, J., Feliciano, C., Ting, J.T., Wang, W., Wells, M.F., Venkatraman, T.N., Lascola, C.D., Fu, Z., and Feng, G. (2011). Shank3 mutant mice display autistic-like behaviours and striatal dysfunction. Nature *472*, 437-442.

Racine, R.J. (1972). Modification of seizure activity by electrical stimulation. II. Motor seizure. Electroencephalogr Clin Neurophysiol *32*, 281-294.

Schevon, C.A., Weiss, S.A., McKhann, G., Jr., Goodman, R.R., Yuste, R., Emerson, R.G., and Trevelyan, A.J. (2012). Evidence of an inhibitory restraint of seizure activity in humans. Nat Commun *3*, 1060.

Schwarz, T. (2013) Release of Neurotransmitters, in Fundamental Neuroscience, 4th ed, Academic Press, 139-161.

Scotland, P., Zhou, D., Benveniste, H., and Bennett, V. (1998). Nervous system defects of AnkyrinB (-/-) mice suggest functional overlap between the cell adhesion molecule L1 and 440-kD AnkyrinB in premyelinated axons. J Cell Biol *143*, 1305-1315.

Takeichi, T., Takarada-Iemata, M., Hashida, K., Sudo, H., Okuda, T., Kokame, K., Hatano, T., Takanashi, M., Funabe, S., Hattori, N.*, et al.* (2011). The effect of Ndrg2 expression on astroglial activation. Neurochem Int *59*, 21-27.

Thiebes, K., Nam, H., Cambronne, X., Shen, R., Glasgow, S., Cho, H., Kwon, J., Goodman, R., Lee, J., Lee, S., and Lee, S.K. (2015). miR-218 is essential to establish motor neuron fate as a downstream effector of Isl1-Lhx3. Nat Commun *2015*, 6:7718.

Vogel-Ciernia, A., Matheos, D.P., Barrett, R.M., Kramar, E.A., Azzawi, S., Chen, Y., Magnan, C.N., Zeller, M., Sylvain, A., Haettig, J.*, et al.* (2013). The neuron-specific chromatin regulatory subunit BAF53b is necessary for synaptic plasticity and memory. Nat Neurosci *16*, 552-561.

Wayman, G.A., Davare, M., Ando, H., Fortin, D., Varlamova, O., Cheng, H.Y., Marks, D., Obrietan, K., Soderling, T.R., Goodman, R.H.*, et al.* (2008). An activity-regulated microRNA controls dendritic plasticity by down-regulating p250GAP. Proc Natl Acad Sci U S A *105*, 9093-9098.

Yang, J.H., Li, J.H., Shao, P., Zhou, H., Chen, Y.Q., and Qu, L.H. (2011). starBase: a database for exploring microRNA-mRNA interaction maps from Argonaute CLIP-Seq and Degradome-Seq data. Nucleic Acids Res *39*, D202-209.

Zanardi, A., Ferrari, R., Leo, G., Maskos, U., Changeux, J.P., and Zoli, M. (2007). Loss of high-affinity nicotinic receptors increases the vulnerability to excitotoxic lesion and decreases the positive effects of an enriched environment. FASEB J *21*, 4028-4037.

Zenisek, D., and Matthews, G. (2000). The role of mitochondria in presynaptic calcium handling at a ribbon synapse. Neuron *25*, 229-237.

Ziviani, E., Lippi, G., Bano, D., Munarriz, E., Guiducci, S., Zoli, M., Young, K.W., and Nicotera, P. (2011). Ryanodine receptor-2 upregulation and nicotine-mediated plasticity. EMBO J *30*, 194-204.

Zovoilis, A., Agbemenyah, H.Y., Agis-Balboa, R.C., Stilling, R.M., Edbauer, D., Rao, P., Farinelli, L., Delalle, I., Schmitt, A., Falkai, P*., et al.* (2011). microRNA-34c is a novel target to treat dementias. EMBO J *30*, 4299-4308.